Flexible Aircraft Gust Load Alleviation with Incremental Nonlinear Dynamic Inversion

Wang, Xuerui; van Kampen, Erik-Jan; Chu, Qiping; De Breuker, Roeland

DOI
10.2514/1.G003980

Publication date
2019

Document Version
Final published version

Published in
Journal of Guidance, Control, and Dynamics: devoted to the technology of dynamics and control

Citation (APA)
Wang, X., van Kampen, E.-J., Chu, Q., & De Breuker, R. (2019). Flexible Aircraft Gust Load Alleviation with Incremental Nonlinear Dynamic Inversion. *Journal of Guidance, Control, and Dynamics: devoted to the technology of dynamics and control*, *42*(7), 1519-1536. https://doi.org/10.2514/1.G003980

JOURNAL OF GUIDANCE, CONTROL, AND DYNAMICS
Vol. 42, No. 7, July 2019

Flexible Aircraft Gust Load Alleviation with Incremental Nonlinear Dynamic Inversion

X. Wang,* E. Van Kampen,† Q. P. Chu,‡ and Roeland De Breuker§
Delft University of Technology, 2629 HS Delft, The Netherlands

DOI: 10.2514/1.G003980

This paper designs an incremental nonlinear dynamic inversion control law for free-flying flexible aircraft, which can regulate rigid-body motions, alleviate gust loads, reduce the wing root bending moment, and suppress elastic modes. By fully exploring the sensor measurements, the model dependency of the proposed control law can be reduced while maintaining desirable robustness, which simplifies the implementation process and reduces the onboard computational load. The elastic states are observed online from accelerometer measurements, with a Padé approximation to model the pure time delay. Theoretical analyses based on the Lyapunov methods and the nonlinear system perturbation theory show that the proposed control has inherent robustness to model uncertainties, external disturbances, and sudden actuator faults. These merits are demonstrated by time-domain simulations in various spatial turbulence and gust fields, as well as by a Monte Carlo study.

Nomenclature

$\boldsymbol{C}_f$	=	matrix of direction cosines between (x_f, y_f, z_f) and (X_E, Y_E, Z_E)
$\boldsymbol{\mathcal{C}}_{uw}$, $\boldsymbol{\mathcal{C}}_{\psi w}$	=	damping matrices for the bending and torsion of the wing
$\boldsymbol{C}_w$	=	matrix of direction cosines between (x_w, y_w, z_w) and (x_f, y_f, z_f)
EI, GJ	=	bending and torsional stiffnesses, N · m^2
$\boldsymbol{E}_f$	=	matrix relating Eulerian velocities to angular quasi velocities
$\boldsymbol{F}$, $\boldsymbol{M}$	=	generalized resultant forces and moments, N and N · m
$\boldsymbol{G}$	=	control effectiveness matrix
$\boldsymbol{\mathcal{K}}_{uw}$, $\boldsymbol{\mathcal{K}}_{\Psi w}$	=	stiffness matrices for the bending and torsion of the wing
$\boldsymbol{M}_r$	=	wing root bending moment, N · m
$\boldsymbol{M}_{\text{st}}$	=	system mass matrix
n_z	=	vertical load factor, m/s^2
$\boldsymbol{p}_{V_f}$, $\boldsymbol{p}_{\omega_f}$, $\boldsymbol{p}_{uw}$, $\boldsymbol{p}_{\psi w}$	=	momentum vectors for aircraft translation, rotation, bending, and torsion
$\boldsymbol{q}$, $\boldsymbol{\xi}$	=	vectors of generalized coordinates for the bending and torsion
$\boldsymbol{R}_f$	=	position vector of the origin of (x_f, y_f, z_f) relative to (X_E, Y_E, Z_E), m
$\boldsymbol{r}_w$	=	nominal position vector of a point on the wing, m
$\boldsymbol{s}$, $\boldsymbol{\eta}$	=	vectors of generalized coordinates for the bending and torsion velocities, m/s and rad/s
$\boldsymbol{u}_w$, $\boldsymbol{\psi}_w$	=	bending and torsion displacements of the wing, m and rad
$\boldsymbol{V}_f$	=	translational velocity vectors of (x_f, y_f, z_f), m/s
$\boldsymbol{x}_r$, $\boldsymbol{x}_e$	=	rigid and elastic states vectors
$\boldsymbol{x}_{rm}$	=	state reference vector
$\Delta\boldsymbol{u}$	=	incremental control input
$\boldsymbol{\theta}_f$	=	Euler angles vector, rad
κ	=	fault indicator
$\boldsymbol{\nu}$	=	virtual control vector
$\boldsymbol{\Phi}$, $\boldsymbol{\Psi}$	=	shape function matrices of the bending and torsion
$\boldsymbol{\omega}_f$	=	angular velocity vector of (x_f, y_f, z_f), rad/s

I. Introduction

WHILE enjoying the benefits provided by lightweight composite materials, aircraft designers are facing the challenges of the accompanying greater structural flexibility. As the structural flexibility increases, not only do the interactions between aerodynamics and structural dynamics become significant but the coupling effects between rigid-body dynamics and structural dynamics are also nonnegligible [1–4]. When a flexible aircraft encounters atmospheric disturbances, both the rigid-body and flexible modes are excited, which reduce pilot handling qualities, degrade passenger ride quality, introduce extra structural loads, and shorten the structural fatigue life. Traditionally, the flight control and structural vibration suppression are performed separately, and notch filters are used to avoid interactions between them. This design approach may be less appropriate for modern flexible aircraft. Instead, an integrated control design, which simultaneously accounts for rigid-body and aeroelastic control, can lead to better overall performance.

The free-flying dynamics of flexible aircraft are nonlinear and time varying (NLTV) [2,5]. The nonlinearities are contributed to by flight dynamics, aeroelasticity, and the inertial couplings between them [2]. Even for a rigid aircraft, when the angle of attack is high or when the aircraft is in transonic flight, the aerodynamics are nonlinear. Under the small deformation assumption, the structural vibration dynamics are described by a series of second-order linear differential equations, and their inertial couplings with rigid-body dynamics are negligible. These can be invalid for highly flexible aircraft, for which the consideration of nonlinearity in flight control design becomes important [6,7].

In the literature of flexible aircraft flight control, it is a common practice to linearize the NLTV system around an equilibrium point, and then execute a model reduction procedure. Based on the resulting low-order and linear time-invariant (LTI) system, the linear quadratic Gaussian (LQG) method was used for gust load alleviation (GLA) in Refs. [8,9] and for flutter suppression in Refs. [10,11]. Although both the linear quadratic regulator (LQR) and the Kalman filter are optimal, as well as their combination, the LQG does not automatically ensure good robustness properties. Linear robust control can improve

Presented as Paper 2018-0774 at the 2018 AIAA Atmospheric Flights Mechanics Conference, Kissimmee, FL, 8–12 January 2018; received 20 July 2018; revision received 19 December 2018; accepted for publication 8 January 2019; published online 28 February 2019.

*Ph.D. Candidate, Control and Simulation Section, Faculty of Aerospace Engineering, Kluyverweg 1, Zuid-Holland; X.Wang-6@tudelft.nl. Student Member AIAA.

†Assistant Professor, Control and Simulation Section, Faculty of Aerospace Engineering, Kluyverweg 1, Zuid-Holland; E.vanKampen@tudelft.nl. Member AIAA.

‡Associate Professor, Control and Simulation Section, Faculty of Aerospace Engineering, Kluyverweg 1, Zuid-Holland; Q.P.Chu@tudelft.nl. Member AIAA.

§Associate Professor, Aerospace Structures and Computational Mechanics, Faculty of Aerospace Engineering, Kluyverweg 1, Zuid-Holland; R.DeBreuker@tudelft.nl. Member AIAA.

the robustness of a closed-loop system. An H_∞ robust controller was designed in Ref. [12] for reducing the wing root bending moment of a very flexible aircraft. In Ref. [7], a mixed norm H_2/H_∞ control was used to alleviate the gust load of a flexible aircraft. However, it was commented in Ref. [13] that LTI model-based robust control could be either marginal or overly conservative in performance and stability robustness. Moreover, to ensure desirable handling qualities over the entire flight envelope, controllers based on LTI models need to be used along with the gain scheduling method, which can be cumbersome and does not guarantee stability robustness [14].

Flexible aircraft control designs considering nonlinearities do exist in the literature. In Ref. [15], the nonlinear dynamic inversion (NDI) method was used to control a high-altitude long-endurance highly flexible aircraft. Because the NDI design uses a nonlinear model, it can be applied in the absence of gain scheduling. Nonetheless, the robustness of NDI is impaired by its model dependency. An adaptive backstepping (ABS) control was designed for an aeroservoelastic system in Ref. [16], in which the plant was parameterized using predefined model structures. However, the unknown parameters are assumed to be constant or slowly time varying in ABS design [17], which limits its applicability. Furthermore, not all the uncertainties and external disturbances can be parameterized and, even if they can, tuning of the resulting design can be tedious. An LTI aeroservoelastic system augmented by a nonlinear perturbation term was regulated by a model reference adaptive control (MRAC) in Ref. [16], in which it was assumed that the perturbation satisfied the matching condition and could be parameterized into the multiplication of regressors and constant parameters. The reference model used in Ref. [16] was also LTI; thus, model updates were necessary when the flight condition changed or when a fault occurred. Because the flight envelope shrinks in faulty conditions [18], enforcing the system to track an LTI model designed in the nominal case can lead to instability. Last, but not least, dynamic equations need to be solved for the parameter adaptation in MRAC, which requires high computational resources, especially for a high-order aeroservoelastic system.

Incremental nonlinear dynamic inversion (INDI) is a nonlinear sensor-based control approach. After its proposal in Ref. [19], its effectiveness has been demonstrated by real-world flight tests on a tail-sitter unmanned aerial vehicle [20], quadrotors [21–23], and even a CS-25 certified passenger aircraft [24]. The stability and robustness of INDI was analyzed in Ref. [25] using Lyapunov methods and a nonlinear system perturbation theory. As compared to the LTI model-based control methods, the gain scheduling technique is not needed by INDI. The uncertainty parameterization process is also omitted in INDI, which removes the slowly time-varying parameter assumption and eliminates the tedious model structure selection procedure. INDI has less model dependency than NDI, ABS, and MRAC, which simplifies its implementation process. The tuning of INDI is straightforward [26]. Being independent of the dynamic parameter update laws, INDI also has lower computational cost.

Although the model dependency of INDI is reduced, its robustness is enhanced by the feedback of state derivatives. The robustness of INDI to model uncertainties has been analyzed in Ref. [25] and evaluated in Refs. [19,27]. By virtue of its sensor-based nature, INDI is able to passively tolerate a wide range of actuator faults and structural damages without using any additional robust or adaptive techniques [28]. As analyzed in Ref. [25], INDI also has inherent robustness to external disturbances. The wind-tunnel tests in Ref. [21] showed that, under the INDI control, a damaged quadrotor with complete loss of a single rotor can resist over 9 m/s of wind disturbance. A rigid aircraft GLA problem was considered in Ref. [29], in which INDI outperformed the LQR control. These merits of INDI inspired the idea of using it to solve the flexible aircraft GLA problem, which has not been addressed in the literature. Due to the complexity of aeroservoelastic systems, several research questions emerge: How do we conduct a reasonable model simplification based on the characteristics of flexible aircraft? How do we make tradeoffs among different control objectives in the framework of INDI? How do we obtain the state derivatives of flexible aircraft? How is the robustness of the control to state estimation errors, external disturbances, sudden faults, and model uncertainties? These questions will be answered in this paper.

The main contributions of this paper are 1) an integrated nonlinear control law for flexible aircraft aiming at rigid-body motion regulation, gust load alleviation, wing root bending moment reduction, and elastic mode suppression; 2) an online optimal state observer with a Padé approximation to model the pure time delay; and 3) theoretical analyses and numerical validations for the robustness of the proposed control to external disturbances, sudden faults, and model uncertainties.

The rest of the paper is organized as follows: Section II presents the models for flexible aircraft and turbulence fields. Section III derives the INDI GLA control law with the simulation results shown and discussed in Sec. IV. The main conclusions are drawn in Sec. V.

II. Flexible Aircraft and Gust Models

A. Flexible Aircraft Equations of Motion

To capture both aerodynamic and inertial coupling effects between the rigid-body and structural dynamics of free-flying flexible aircraft, the dynamic equations derived in quasi coordinates [2] are adopted in this paper. The flexible wings are modeled as cantilever beams undergoing bending and torsional deformations. The remaining components [namely, fuselage and empennage (horizontal and vertical tails)] are assumed to be rigid. A set of body-fixed axes (O_i, x_i, y_i, z_i) with $i = f, w, e$ are attached to the undeformed aircraft as shown by Fig. 1.

The kinematic equations of this flexible aircraft are

$$\dot{\boldsymbol{R}}_f = \boldsymbol{C}_f^T \boldsymbol{V}_f, \qquad \dot{\boldsymbol{\theta}}_f = \boldsymbol{E}_f^{-1} \boldsymbol{\omega}_f \tag{1}$$

where $\boldsymbol{V}_f$ and $\boldsymbol{\omega}_f$ represent the (O_f, x_f, y_f, z_f) axes translational and rotational velocities, whereas $\boldsymbol{R}_f$ and $\boldsymbol{\theta}_f$ indicate the position and Euler angles of the (O_f, x_f, y_f, z_f) axes relative to the inertia frame (O, X_E, Y_E, Z_E). O_f can be an arbitrary fixed point in the aircraft symmetrical plane, and there is no requirement on the coincidence of O_f and the center of mass. $\boldsymbol{C}_f(\phi, \theta, \psi)$ is the rotation transformation matrix from the inertial frame (O, X_E, Y_E, Z_E) to (O_f, x_f, y_f, z_f). The $\boldsymbol{E}_f(\phi, \theta)$ matrix links angular velocities $\boldsymbol{\omega}_f$ to Eulerian velocities $\dot{\boldsymbol{\theta}}_f$. For the flexible wings, the Galerkin method is used to discretize the bending displacements $\boldsymbol{u}_w$ and torsion angles $\boldsymbol{\psi}_w$ in the modal form as

$$\begin{aligned} \boldsymbol{u}_w(\boldsymbol{r}_w, t) &= \boldsymbol{\Phi}(\boldsymbol{r}_w)\boldsymbol{q}(t), \quad \dot{\boldsymbol{q}}(t) = \boldsymbol{s}(t) \\ \boldsymbol{\psi}_w(\boldsymbol{r}_w, t) &= \boldsymbol{\Psi}(\boldsymbol{r}_w)\boldsymbol{\xi}(t), \quad \dot{\boldsymbol{\xi}}(t) = \boldsymbol{\eta}(t) \end{aligned} \tag{2}$$

where $\boldsymbol{\Phi}(\boldsymbol{r}_w)$ and $\boldsymbol{\Psi}(\boldsymbol{r}_w)$ are bending and torsion shape function matrices, respectively. Also, $\boldsymbol{q}(t)$ and $\boldsymbol{\xi}(t)$ are the generalized coordinate vectors. The elastic deformations can also be discretized using the finite element method, and the resulting equations are in the

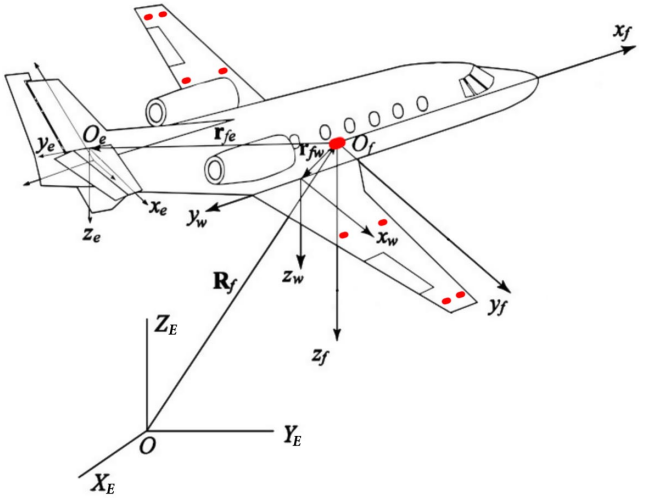

Fig. 1 Coordinate system definition [2].

same form as Eq. (2). Denote the linear momentum of the aircraft as $\boldsymbol{p} = [\,\boldsymbol{p}_{V_f}^T \quad \boldsymbol{p}_{\omega_f}^T \quad \boldsymbol{p}_{uw}^T \quad \boldsymbol{p}_{\psi w}^T\,]^T$, which also equals $\boldsymbol{M}_{\text{st}}\boldsymbol{V}$, where $\boldsymbol{V} = [\,\boldsymbol{V}_f^T \quad \boldsymbol{\omega}_f^T \quad \boldsymbol{s}^T \quad \boldsymbol{\eta}^T\,]^T$ is a velocity vector and $\boldsymbol{M}_{\text{st}}$ is a time-varying mass matrix as a function of elastic deformations. The translational, rotational, bending, and torsion dynamics of the flexible aircraft are [2]

$$\begin{aligned}
\dot{\boldsymbol{p}}_{v_f} &= -\tilde{\boldsymbol{\omega}}\boldsymbol{p}_{v_f} + \boldsymbol{F}\\
\dot{\boldsymbol{p}}_{\omega_f} &= -\tilde{\boldsymbol{V}}_f\boldsymbol{p}_{v_f} - \tilde{\boldsymbol{\omega}}\boldsymbol{p}_{\omega_f} + \boldsymbol{M}\\
\dot{\boldsymbol{p}}_{uw} &= \partial\mathcal{T}/\partial\boldsymbol{q} - \boldsymbol{K}_{uw}\boldsymbol{q} - \boldsymbol{C}_{uw}\boldsymbol{s} + \boldsymbol{Q}\\
\dot{\boldsymbol{p}}_{\psi w} &= -\boldsymbol{K}_{\psi w}\boldsymbol{\xi} - \boldsymbol{C}_{\psi w}\boldsymbol{\eta} + \boldsymbol{\Theta}
\end{aligned} \tag{3}$$

in which a tilde $(\tilde{\cdot})$ represents the skew-symmetric matrix of a vector. Also, $\partial\mathcal{T}/\partial\boldsymbol{q}$ includes the Coriolis and centrifugal forces of the wing:

$$\mathcal{K}_{uw} = \int \text{EI}(\boldsymbol{\Phi}'')^T\boldsymbol{\Phi}''\,\text{d}x, \quad \mathcal{K}_{\Psi w} = \int \text{GJ}(\boldsymbol{\Psi}'')^T\boldsymbol{\Psi}''\,\text{d}x$$

in which EI and GJ are the bending and torsion stiffnesses, respectively. The structural damping matrices $\mathcal{C}_{uw}$ and $\mathcal{C}_{\Psi w}$ are assumed to be proportional to $\mathcal{K}_{uw}$ and $\mathcal{K}_{\psi w}$. On the right–hand side of Eq. (3), the total force $\boldsymbol{F}$, the total moment $\boldsymbol{M}$, and the generalized elastic forces $\boldsymbol{Q}$ and $\boldsymbol{\Theta}$ are calculated from the distributed forces by means of virtual work [2]. These distributed forces contain the aerodynamic, gravitational, and thrust forces.

B. Unsteady Aerodynamic Models

In this paper, the unsteady aerodynamics of the wing and tails are modeled using the modified strip theory. In this approach, the considered lifting surface is discretized into a series of undeformable strips. The aerodynamic force and moment on each strip are calculated using its steady-flow aerodynamic properties and the unsteady aerodynamic theories for a two-dimensional (2-D) airfoil. Consider a 2-D airfoil exposed to disturbed atmosphere with three degrees of freedom: heave h, pitching around the elastic axis ϵ, and a flap deflection δ. The geometric parameters and the positive directions of movements are indicated in Fig. 2. It is worth noting that h and ϵ contain the contributions from both rigid-body and structural motions. In incompressible flow, the sectional lift coefficient and pitching moment coefficient around the elastic axis are formulated as

$$\begin{aligned}
C_L &= C_L^{c,h\epsilon} + C_L^{\text{nc},h\epsilon} + C_L^{c,\delta} + C_L^{\text{nc},\delta} + C_L^{c,g}\\
C_m &= C_m^{c,h\epsilon} + C_m^{\text{nc},h\epsilon} + C_m^{c,\delta} + C_m^{\text{nc},\delta} + C_m^{c,g}
\end{aligned} \tag{4}$$

In Eq. (4), the superscripts c and nc, respectively, indicate the circulatory and noncirculatory contributions. The circulatory terms are caused by the vorticity in the flow, which is time-history dependent. The noncirculatory terms result from the change in momentum of the surrounding air caused by the airfoil motions and flap deflections. In incompressible flow, the noncirculatory contributions are instant and not subject to a time-history effect [30]. The superscripts $h\epsilon$, δ, and g, respectively, denote the contributions from the airfoil motions, flap deflections, and atmospheric disturbances. Using the expressions of Theodorsen [31], the circulatory terms due to airfoil motions are as follows:

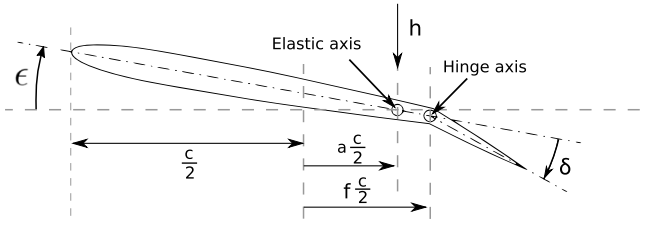

Fig. 2 2-D airfoil with a trailing-edge flap.

$$C_L^{c,h\epsilon} = C_{L_\alpha}^{\text{SF}}C(k)\alpha_{3/4}, \quad C_m^{c,h\epsilon} = \left(\frac{1}{4}+\frac{a}{2}\right)C_L^{c,h\epsilon} \tag{5}$$

where $C_{L_\alpha}^{\text{SF}}$ is the lift curve slope in steady flow, which includes a compressibility correction using the Prandtl–Glauert factor. It is noteworthy that Theodorsen considered thin airfoils, thus the lift curve slope $C_{L_\alpha}^{\text{SF}}$ was assumed to be 2π [31]. In this paper, more general expressions are used in Eq. (5).

$$\alpha_{3/4} = \epsilon + \frac{\dot{h}}{V} + \frac{c}{2V}\left(\frac{1}{2}-a\right)\dot{\epsilon}$$

is the angle of attack at the three-quarter-chord. $C(k)$ is the Theodorsen's function, where $k = \omega c/2V$ is the reduced frequency [31]. For an airfoil with a lift curve slope of $C_{L_\alpha}^{\text{SF}}$ in steady flow, the noncirculatory coefficients due to airfoil motions are as follows [31]:

$$\begin{aligned}
C_L^{\text{nc},h\epsilon} &= \frac{C_{L_\alpha}^{\text{SF}}}{2\pi}\frac{c}{4V}\left(\dot{\epsilon} + \frac{\ddot{h}}{V} - a\frac{c}{2V}\ddot{\epsilon}\right),\\
C_m^{\text{nc},h\epsilon} &= -\frac{C_{L_\alpha}^{\text{SF}}}{2\pi}\frac{c}{8V}\left(\left(\frac{1}{2}-a\right)\dot{\epsilon} - a\frac{\ddot{h}}{V} + \frac{c}{2V}\left(\frac{1}{8}+a^2\right)\ddot{\epsilon}\right)
\end{aligned} \tag{6}$$

The circulatory terms contributed by flap deflections also have time-history effects; they are given as

$$C_L^{c,\delta} = C_{L_\alpha}^{\text{SF}}C(k)\left(\frac{T_{10}}{\pi}\delta + \frac{T_{11}}{2\pi}\frac{c}{2V}\dot{\delta}\right), \quad C_m^{c,\delta} = \left(\frac{1}{4}+\frac{a}{2}\right)C_L^{c,\delta} \tag{7}$$

where T_{10} and T_{11} are constant geometric parameters depending on the hinge position [31]. The noncirculatory terms contributed by the flap are functions of δ, $\dot{\delta}$, and $\ddot{\delta}$. Their specific expressions can be found in Ref. [31]. $C(k)$ in Eq. (7) is the same as used in Eq. (5), which depends on the reduced frequency k. However, this formulation is less suitable for simulating aircraft maneuvers under random turbulence excitations in the time domain. Wagner's function, which gives the lift response to a step change in angle of attack due to airfoil motions, is the time-domain counterpart of Theodorsen's function [32]. An exponential approximation of Wagner's function is

$$\phi(\tau) = 1 - 0.165e^{-0.0455\tau} - 0.335e^{-0.3\tau}$$

where $\tau = 2Vt/c$ is a nondimensional time variable [33]. On the other hand, the unsteady responses of an airfoil to a unit sharp-edged gust are given by the Küssner function, which is exponentially approximated as $\psi_g(\tau) = 1 - 0.5e^{-0.13\tau} - 0.5e^{-\tau}$ [32]. Both $\phi(\tau)$ and $\psi_g(\tau)$ are in the form of $f(\tau) = 1 - a_1e^{-b_1\tau} - a_2e^{-b_2\tau}$. Using the Duhamel's integral, a system that has an indicial response function $f(\tau)$ can be realized in the control canonical form as follows:

$$\begin{aligned}
\begin{bmatrix}\dot{x}_{a_1}\\ \dot{x}_{a_2}\end{bmatrix} &= \begin{bmatrix}0 & 1\\ -\left(\frac{2V}{c}\right)^2 b_1b_2 & -\left(\frac{2V}{c}\right)(b_1+b_2)\end{bmatrix}\begin{bmatrix}x_{a_1}\\ x_{a_2}\end{bmatrix} + \begin{bmatrix}0\\1\end{bmatrix}u\\
y &= \left[(a_1+a_2)b_1b_2\left(\frac{2V}{c}\right)^2, (a_1b_1+a_2b_2)\left(\frac{2V}{c}\right)\right]\begin{bmatrix}x_{a_1}\\ x_{a_2}\end{bmatrix}\\
&\quad + (1-a_1-a_2)u
\end{aligned} \tag{8}$$

Substituting the parameters of $\phi(\tau)$ into Eq. (8) and choosing

$$u = \alpha_{3/4} + \left(\frac{T_{10}}{\pi}\delta + \frac{T_{11}}{2\pi}\frac{c}{2V}\dot{\delta}\right)$$

then, based on Eqs. (5) and (7), the circulatory lift coefficient caused by arbitrary airfoil motions and flap deflections is $C_L^{c,h\epsilon} + C_L^{c,\delta} = C_{L_\alpha}^{\text{SF}}y$. The corresponding circulatory moment coefficient equals $C_{L_\alpha}^{\text{SF}}y$ multiplied with $\frac{1}{4}+\frac{a}{2}$ [Eqs. (5) and (7)].

On the other hand, consider that the airfoil encounters an arbitrary vertical gust input $w_g(t)$ on the leading edge. Substituting the parameters of $\psi_g(\tau)$ into Eq. (8), then the gust-induced lift coefficient $C_L^{c,g}$ equals $C_{L_\alpha}^{\mathrm{SF}} y$ when the input u equals $\mathrm{atan}(w_g(t)/V)$. Analogously, $C_m^{c,g}$ in Eq. (4) equals $(0.25 + 0.5\mathrm{a})C_L^{c,g}$.

Note that x_{a_1} and x_{a_2} in Eq. (8) are known as the aerodynamic lag states. In view of the preceding derivations, four aerodynamic lag states are needed by each strip. Two of them are used for modeling the time-history-dependent effects caused by motions and flap deflections, and the other two are used to model unsteady gust responses.

This paper considers viscous flow, and the sectional drag coefficient is modeled as

$$C_D = C_{D_0} + k_D\left(C_L^{c,h\epsilon} + C_L^{c,\delta} + C_L^{c,g}\right)^2$$

C_{D_0} is the drag coefficient corresponding to zero lift. Only the circulatory part of the lift contributes to the quadratic drag [32]. Using the sectional aerodynamic coefficients C_L, C_D, and C_m the distributed aerodynamic forces and moments can be calculated.

C. Gust and Turbulence Models

Two methods are often used to model atmospheric disturbances, namely, the stochastic continuous turbulence and the deterministic discrete gust. The continuous turbulence is often simplified into a stationary, homogeneous, isotropic stochastic process with Gaussian distribution. The power spectral density of the two commonly used turbulence models, which are the Dryden (denoted by subscript D_w) and von Kármán models (denoted by subscript vKw), are, respectively, given by [34]

$$\Phi_{Dw}(\omega) = \sigma^2 \frac{L_g}{\pi V}\frac{1 + 3(L_g\omega/V)^2}{[1 + (L_g\omega/V)^2]^2},$$
$$\Phi_{vKw}(\omega) = \sigma^2 \frac{L_g}{\pi V}\frac{1 + \frac{8}{3}(a(L_g\omega/V))^2}{[1 + (a(L_g\omega/V))^2]^{11/6}} \tag{9}$$

where ω is the angular frequency, L_g is the turbulence scale length, and σ is the turbulence intensity. Constant $a = 1.339$, and V is the aircraft speed. Although the von Kármán model better fits the available experimental and theoretical data, especially in the high-frequency range [35], its irrational spectra require approximate difference equations to generate turbulence velocities in the time domain. As an alternative, it can be realized in the two-dimensional spatial domain based on the 2-D von Kármán spectrum [35]

$$S_{w_g w_g}(\Omega_x, \Omega_y) = \frac{4\sigma^2(aL_g)^4}{9\pi}\frac{\Omega_x^2 + \Omega_y^2}{[1 + (a\Omega_x L_g)^2 + (a\Omega_y L_g)^2]^{7/3}} \tag{10}$$

where Ω_x and Ω_y are the spatial frequencies along the X_E and Y_E directions. The vertical turbulence velocity w_g as a function of the spatial position (X_E, Y_E) is calculated as

$$w_g(X_E, Y_E) = \mathcal{F}^{-2}\left\{\sqrt{S_{w_g w_g}(\Omega_x, \Omega_y)}\mathcal{F}^2\{w_n(X_E, Y_E)\}\right\} \tag{11}$$

in which $w_n(X_E, Y_E)$ represents the 2-D Gauss white noise generated in the spatial domain. $\mathcal{F}^{-2}$ represents the 2-D inverse Fourier transform, whereas $\mathcal{F}^2$ denotes the 2-D Fourier transform. For more details about this 2-D realization, Ref. [36] is recommended for readers. In this paper, the external disturbances are assumed to be symmetrical to the aircraft (O_f, x_f, y_f) plane, whereas the turbulence velocities vary along the wing span. For example, a realization of the 2-D symmetrical von Kármán moderate turbulence field with $L_g =$ 762 m and $\sigma = 1.5$ m/s is shown in Fig. 3. This realization can be verified by comparing the covariance function of the simulated field with its theoretical values [35].

The rational spectra of the Dryden model allow it to be directly realized in the time domain by passing a white noise through a filter given by Eq. (12). This filter will be used in the state estimation process (Sec. III.C):

$$H_{Dw}(s) = \sigma\sqrt{\frac{L_g}{\pi V}}\frac{1 + (\sqrt{3}L_g/V)s}{(1 + (L_g/V)s)^2} \tag{12}$$

The "1 − cos" gust model can more precisely capture the solitary gust feature, as compared to the sharp-edged and the ramped gust models. A 1 − cos gust is defined as Eq. (13) and can be broadened into symmetric w_{g_s} and asymmetric w_{g_a} gust fields, as described by Eq. (14):

$$w_g = \frac{w_m}{2}\left(1 - \cos\frac{2\pi X_E}{\lambda_x}\right) \tag{13}$$

$$w_{g_s} = \frac{w_m}{4}\left(1 - \cos\frac{2\pi X_E}{\lambda_x}\right)\left(1 - \cos\frac{2\pi Y_E}{\lambda_y}\right),$$
$$w_{g_a} = \frac{w_m}{2}\left(1 - \cos\frac{2\pi X_E}{\lambda_x}\right)\sin\frac{2\pi Y_E}{\lambda_y} \tag{14}$$

where w_m represents the maximum gust velocity, and λ_x and λ_y refer to the gust lengths in the X_E and Y_E directions, respectively. An example of a symmetric gust field is given by Fig. 4, in which the parameters of the first gust w_{g_1} are $\lambda_{x_1} = \lambda_{y_1} = 100$ m and $w_{m_1} =$ 5 m/s and of the second gust w_{g_2} are $\lambda_{x_2} = \lambda_{y_2} = 180$ m and $w_{m_2} = 5$ m/s.

During time-domain simulations, the flexible aircraft flies through the 2-D spatial turbulence and gust fields. For each aerodynamic strip, the local vertical gust velocity w_g is independently interpolated using the spatial location of the airfoil leading edge. In this way, the gust penetration effect [35] is naturally captured. In short, this effect means that the gust met by the wings at the current time instant will only be encountered by the tail after a short time period.

III. Flexible Aircraft Gust Load Alleviation Control

A. Incremental Nonlinear Dynamic Inversion Control

Considering a nonlinear control-affine system,

$$\dot{\boldsymbol{x}} = \boldsymbol{f}(\boldsymbol{x}, \kappa(t)) + \boldsymbol{G}(\boldsymbol{x}, \kappa(t))\boldsymbol{u} + \boldsymbol{d}(t) \tag{15}$$

where $\boldsymbol{d}$ represents a bounded external disturbance vector. To indicate a sudden fault at $t = t_f$ during flight, $\kappa(t) \in \mathbb{R}$ is designed as a step

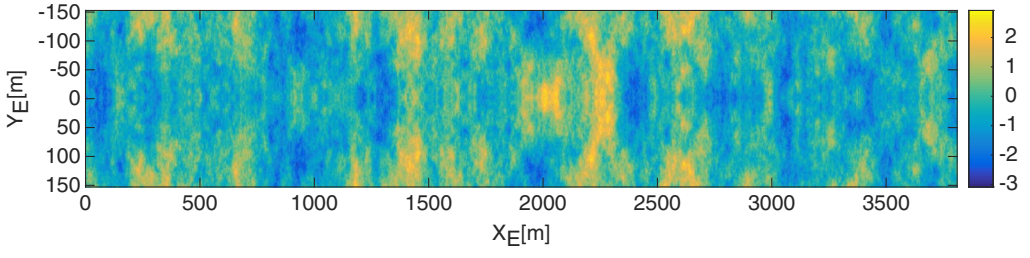

Fig. 3 2-D symmetrical von Kármán vertical turbulence field ($L_g = 762$ m, and $\sigma = 1.5$ m/s).

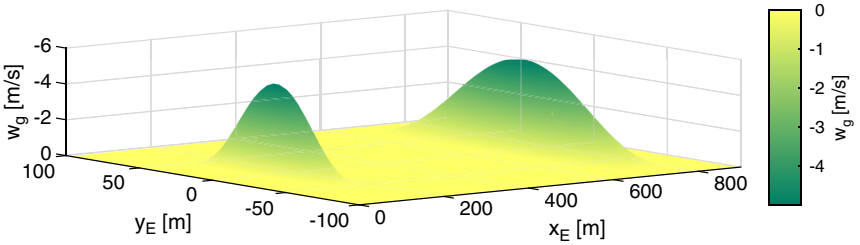

Fig. 4 2-D symmetrical 1 − cos vertical gust field.

function, with $t < t_f$, $\kappa = 0$ indicating the fault-free case and $t \geq t_f$, $\kappa = 1$ denoting the postfault condition.

Assumption 1: The partial derivatives of $\boldsymbol{f}$ and $\boldsymbol{G}$ in Eq. (15) with respect to $\boldsymbol{x}$ up to any order are bounded.

Expanding $\boldsymbol{f}$ and $\boldsymbol{G}$ as

$$\boldsymbol{f} = \bar{\boldsymbol{f}} + (\boldsymbol{f}_f - \bar{\boldsymbol{f}})\kappa + \hat{\boldsymbol{f}}, \qquad \boldsymbol{G} = \bar{\boldsymbol{G}} + (\boldsymbol{G}_f - \bar{\boldsymbol{G}})\kappa + \hat{\boldsymbol{G}} \tag{16}$$

where $\bar{\boldsymbol{f}}$ and $\bar{\boldsymbol{G}}$ are the nominal dynamics used for controller design, $\boldsymbol{f}_f$ and $\boldsymbol{G}_f$ denote the postfault dynamics, and $\hat{\boldsymbol{f}}$ and $\hat{\boldsymbol{G}}$ represent the model uncertainties as continuous functions of $\boldsymbol{x}$. Take the first-order Taylor series expansion of Eq. (15) around the condition at $t - \Delta t$ (denoted by the subscript 0) as follows:

$$\begin{aligned}\dot{\boldsymbol{x}} &= \dot{\boldsymbol{x}}_0 + \boldsymbol{G}(\boldsymbol{x}_0, \kappa_0)\Delta\boldsymbol{u} + \left.\frac{\partial[\boldsymbol{f}(\boldsymbol{x},\kappa) + \boldsymbol{G}(\boldsymbol{x},\kappa)\boldsymbol{u}]}{\partial \boldsymbol{x}}\right|_0 \Delta\boldsymbol{x} \\ &+ \left.\frac{\partial[\boldsymbol{f}(\boldsymbol{x},\kappa) + \boldsymbol{G}(\boldsymbol{x},\kappa)\boldsymbol{u}]}{\partial \kappa}\right|_0 \Delta\kappa + \Delta\boldsymbol{d} + \mathcal{O}(\Delta\boldsymbol{x}^2) \\ &\triangleq \dot{\boldsymbol{x}}_0 + \boldsymbol{G}(\boldsymbol{x}_0, \kappa_0)\Delta\boldsymbol{u} + \Delta\boldsymbol{d} + \boldsymbol{\delta}(\boldsymbol{x}, \kappa, \Delta t)\end{aligned} \tag{17}$$

In the preceding equation, $\Delta\boldsymbol{x} = \boldsymbol{x} - \boldsymbol{x}_0$ and $\Delta\boldsymbol{u} = \boldsymbol{u} - \boldsymbol{u}_0$, respectively, denote the variations of the states and control inputs in one incremental time step Δt. $\Delta\kappa = \kappa - \kappa_0$ denotes the changes of the fault indicator κ, whereas $\Delta\boldsymbol{d} = \boldsymbol{d} - \boldsymbol{d}_0$ denotes the variations of the external disturbances $\boldsymbol{d}$ in Δt. The remainder term $\mathcal{O}(\Delta\boldsymbol{x}^2)$ is only a function of $\Delta\boldsymbol{x}^2$ because, according to Eqs. (15) and (16), $\partial^i\dot{\boldsymbol{x}}/\partial\boldsymbol{u}^i = 0$, $\partial^i\dot{\boldsymbol{x}}/\partial\boldsymbol{d}^i = 0$, and $\partial^i\dot{\boldsymbol{x}}/\partial\kappa^i = 0$ for all $i \geq 2$. Use the nominal system control effectiveness matrix $\bar{\boldsymbol{G}}(\boldsymbol{x})$ to design the INDI control increment as $\Delta\boldsymbol{u} = \bar{\boldsymbol{G}}^{-1}(\boldsymbol{x})(\boldsymbol{\nu} - \dot{\boldsymbol{x}}_0)$, where $\boldsymbol{\nu}$ is the virtual control. Then, based on Eq. (17), the closed-loop system dynamics under INDI control are as follows:

$$\begin{aligned}\dot{\boldsymbol{x}} &= \dot{\boldsymbol{x}}_0 + \boldsymbol{G}\bar{\boldsymbol{G}}^{-1}(\boldsymbol{\nu} - \dot{\boldsymbol{x}}_0) + \Delta\boldsymbol{d} + \boldsymbol{\delta}(\boldsymbol{x}, \kappa, \Delta t) \\ &= \boldsymbol{\nu} + (\boldsymbol{G} - \bar{\boldsymbol{G}})\Delta\boldsymbol{u} + \Delta\boldsymbol{d} + \boldsymbol{\delta}(\boldsymbol{x}, \kappa, \Delta t) \triangleq \boldsymbol{\nu} + \boldsymbol{\varepsilon}_{\text{indi}}\end{aligned} \tag{18}$$

Note that $\boldsymbol{\varepsilon}_{\text{indi}}$ in Eq. (18) is a nonlinear perturbation term remaining in the closed-loop system, which is caused by model mismatches, external disturbances, and sudden faults. Using Eq. (16), $\boldsymbol{\delta}(\boldsymbol{x}, \kappa, \Delta t)$ in $\boldsymbol{\varepsilon}_{\text{indi}}$ is further derived as follows:

$$\boldsymbol{\delta}(\boldsymbol{x}, \kappa, \Delta t) = \boldsymbol{\delta}_b(\boldsymbol{x}, \Delta t) + \boldsymbol{\delta}_d(\boldsymbol{x}, \Delta t)\kappa_0 + \boldsymbol{\delta}_\kappa(\boldsymbol{x})\Delta\kappa \tag{19}$$

where

$$\begin{aligned}\boldsymbol{\delta}_b(\boldsymbol{x}, \Delta t) &= \left.\frac{\partial[\bar{\boldsymbol{f}} + \hat{\boldsymbol{f}} + (\bar{\boldsymbol{G}} + \hat{\boldsymbol{G}})\boldsymbol{u}]}{\partial \boldsymbol{x}}\right|_0 \Delta\boldsymbol{x} + \mathcal{O}(\Delta\boldsymbol{x}^2) \\ \boldsymbol{\delta}_d(\boldsymbol{x}, \Delta t) &= \left.\frac{\partial[(\boldsymbol{f}_f - \bar{\boldsymbol{f}}) + (\boldsymbol{G}_f - \hat{\boldsymbol{G}})\boldsymbol{u}]}{\partial \boldsymbol{x}}\right|_0 \Delta\boldsymbol{x} \\ \boldsymbol{\delta}_\kappa(\boldsymbol{x}) &= \left[(\boldsymbol{f}_f - \bar{\boldsymbol{f}}) + (\boldsymbol{G}_f - \bar{\boldsymbol{G}})\boldsymbol{u}\right]\Big|_0\end{aligned} \tag{20}$$

Proposition 1: Under Assumption 1, if $\|I - \boldsymbol{G}\bar{\boldsymbol{G}}^{-1}\| \leq \bar{b} < 1$ for all t, and if $\boldsymbol{\delta}_\kappa(\boldsymbol{x})$ is bounded when $t_f \leq t \leq t_f + \Delta t$, for a sufficiently high sampling frequency, $\boldsymbol{\varepsilon}_{\text{indi}}$ given by Eq. (18) is ultimately bounded.

Proof: Because $\boldsymbol{x}$ is continuously differentiable,

$$\lim_{\Delta t \to 0}\|\Delta\boldsymbol{x}\| = 0$$

Therefore, under Assumption 1, the perturbation terms satisfy

$$\lim_{\Delta t \to 0}\|\boldsymbol{\delta}_b(\boldsymbol{x}, \Delta t)\| = 0 \quad \text{and} \quad \lim_{\Delta t \to 0}\|\boldsymbol{\delta}_d(\boldsymbol{x}, \Delta t)\| = 0$$

Equivalently [25],

$$\begin{aligned}&\forall\bar{\delta}_\varepsilon > 0, \exists\overline{\Delta t} > 0, \\ &\text{such that } \forall\Delta t \in (0, \overline{\Delta t}], \|\boldsymbol{\delta}_b(\boldsymbol{x}, \Delta t)\| \leq \bar{\delta}_\varepsilon, \|\boldsymbol{\delta}_d(\boldsymbol{x}, \Delta t)\| \leq \bar{\delta}_\varepsilon\end{aligned}$$

In other words, there exists a Δt that ensures the boundedness of both $\boldsymbol{\delta}_b(\boldsymbol{x}, \Delta t)$ and $\boldsymbol{\delta}_d(\boldsymbol{x}, \Delta t)$. Also, these bounds can be further diminished by reducing the sampling interval. Moreover, because $\Delta\kappa$ is only nonzero for $t_f \leq t < t_f + \Delta t$, then $\boldsymbol{\delta}_\kappa\Delta\kappa$ is bounded if, during the short time interval, $\boldsymbol{\delta}_\kappa(\boldsymbol{x})$ is bounded. Denote the bound of the entire perturbation term $\boldsymbol{\delta}(\boldsymbol{x}, \kappa, \Delta t)$ as $\bar{\delta}$. Because the virtual control is continuous in time, similarly, there exists a Δt such that the variations of $\boldsymbol{\nu}$ in one time step are bounded. Denote this bound as $\|\boldsymbol{\nu} - \boldsymbol{\nu}_0\| \leq \overline{\Delta\nu}$. For bounded external disturbances in the physical world, their variations in Δt are also bounded. Denote $\|\boldsymbol{d} - \boldsymbol{d}_0\| \leq \overline{\Delta d}$. Analogous to the proof for theorem 1 in Ref. [28], it can be proved recursively that $\boldsymbol{\varepsilon}_{\text{indi}}$ in Eq. (18) is bounded at each time step, and it is ultimately bounded by

$$\bar{\varepsilon}_{\text{indi}} = \frac{\bar{b}\,\overline{\Delta\nu} + \bar{\delta} + \overline{\Delta d}}{1 - \bar{b}}$$

□

The virtual control $\boldsymbol{\nu}$ can be designed for different control purposes (e.g., command tracking, state stabilization, etc. [25]). Consider a command tracking problem, where the first-order time derivative of the reference vector $\boldsymbol{x}_{\text{ref}}$ is assumed to be bounded and piecewise continuous.

Proposition 2: If $\|\boldsymbol{\varepsilon}_{\text{indi}}\| \leq \bar{\varepsilon}_{\text{indi}}$ for all $\boldsymbol{x} \in \mathbb{R}^n$, and design $\boldsymbol{\nu} = \dot{\boldsymbol{x}}_{\text{ref}} + \boldsymbol{K}_p(\boldsymbol{x}_{\text{ref}} - \boldsymbol{x})$, where $\boldsymbol{K}_p$ is a positive definite gain matrix, then the tracking error $\boldsymbol{e} = \boldsymbol{x}_{\text{ref}} - \boldsymbol{x}$ for the system given by Eq. (18) is globally ultimately bounded by a class $\mathcal{K}$ function of $\bar{\varepsilon}_{\text{indi}}$.

Proof: This proposition can be proved by considering a candidate Lyapunov function $V = (\boldsymbol{x}_{\text{ref}} - \boldsymbol{x})^T(\boldsymbol{x}_{\text{ref}} - \boldsymbol{x})$ and using lemma A.3 and proposition B.1 in Ref. [25]. □

The INDI control is featured by its robustness to model mismatches and reduced model dependency. For rigid aircraft control, the estimated control effectiveness matrix $\bar{\boldsymbol{G}}$ is the only model information needed by INDI. $\bar{\boldsymbol{G}}$ can be different from the real $\boldsymbol{G}$, and Proposition 1 only requires a diagonally dominant structure of $\boldsymbol{G}\bar{\boldsymbol{G}}^{-1}$. Even though the controller is independent of $\boldsymbol{f}(\boldsymbol{x})$, its robustness is improved by the feedback of $\dot{\boldsymbol{x}}_0$. As can be seen from Proposition 1, only the disturbance increment $\overline{\Delta d}$ is perturbing the closed-loop system, which is smaller than the bound of $\boldsymbol{d}$ when high sampling frequency is used. The model uncertainty related terms

$\boldsymbol{\delta}_b(\boldsymbol{x}, \Delta t)$ and $\boldsymbol{\delta}_d(\boldsymbol{x}, \Delta t)$ becomes negligible under a sufficiently high sampling frequency. When a sudden fault occurs, the term $\boldsymbol{\delta}_\kappa(\boldsymbol{x})\Delta\kappa$ is only nonzero during a short time interval. For $t \geq t_f + \Delta t$, the main influences of the fault have already been included in the measurements/estimations of $\dot{\boldsymbol{x}}_0$. In the presence of model uncertainties, external disturbances, sudden faults, and even structural damages, $\boldsymbol{\epsilon}_{\text{indi}}$ has a smaller bound than the bound on the remaining perturbation term in nonlinear dynamic inversion control [28]. As a consequence, the ultimate bound of the tracking errors under INDI control is also smaller (Proposition 2).

B. INDI for Flexible Aircraft GLA

The flexible aircraft dynamics given by Eqs. (1) and (3) coupled with unsteady aerodynamics (Sec. II.B) are nonlinear and of high order. For an aircraft model with m_e elastic modes and n_a aerodynamic strips, there are six kinematic states, six states for $\boldsymbol{p}_{V_f}$ and $\boldsymbol{p}_{\omega_f}$, m_e states for $\boldsymbol{p}_{uw}$ and $\boldsymbol{p}_{\psi w}$, m_e states for $\boldsymbol{q}$ and $\boldsymbol{\xi}$ in Eq. (2), and $4n_a$ aerodynamic lag states (Sec. II.B). To reduce the computational load of the onboard controller, and to ensure the observability of the system, it is beneficial to reduce the number of states in the model used for control design. Therefore, a reduced-order nonlinear flexible aircraft model is established, for which the kinematic and dynamic equations are still given by Eqs. (1) and (3), but only the first $m_{e'} < m_e$ structural modes are included. The dynamics of the remaining $m_e - m_{e'}$ modes are viewed as singular perturbations [14,25] to the system. This is reasonable because the high-frequency structural modes are more damped, and they are less coupled with the rigid-body modes. The gust-related $2n_a$ aerodynamic lag states are not needed in this reduced-order model because gust inputs are viewed as external disturbances by the controller, and they are uncorrelated with system dynamics. The other $2n_a$ aerodynamic lag states related to motions are also viewed as singular perturbations to the system [14,25]. The noncirculatory aerodynamic terms do not increase the order of the system; thus, they are viewed as regular perturbations [25,37]. This process reduces the number of states from $12 + 2m_e + 4n_a$ to $12 + 2m_{e'}$, and it reduces the model information available to the controller. The characteristics of the full- and reduced-order models will be compared in Sec. IV.A. The reduced-order model will be used to design the INDI GLA control law. This control law will be validated using the full-order model in Sec. IV.D.

Define the rigid-body states as $\boldsymbol{x}_r = [\,\boldsymbol{V}_f^T \quad \boldsymbol{\omega}_f^T\,]^T$ and the elastic states as $\boldsymbol{x}_e = \boldsymbol{H}[\,\boldsymbol{q}^T \quad \boldsymbol{\xi}^T\,]^T$. $\boldsymbol{H}$ is a boolean selection matrix to choose part of the structural modes for control. Consider the dynamics of the reduced-order model [Eq. (3)], and take the first-order Taylor series expansion as follows:

In the preceding equations, the control vector is defined as $\boldsymbol{u} = [\delta_{a_s}, \delta_{a_a}, \delta_e, \delta_r]^T$. Note that δ_{a_s} and δ_{a_a}, respectively, denote the symmetrical and asymmetrical aileron deflections. Also, δ_e indicates the elevator deflections, whereas δ_r represents the rudder deflections. Lastly, $\boldsymbol{\epsilon}_i$, $i = 1, 2, 3, 4$ includes the $\Delta\kappa$-related terms, the disturbance variations $\Delta\boldsymbol{d}$, and the higher-order terms in Eq. (17).

Based on the proof of Proposition 1, the norm of the state variation $\Delta\boldsymbol{x}$-related terms vanish as Δt approaches zero. In practice, the sampling frequency is constrained by the hardware. For a given Δt, the value of $\boldsymbol{\delta}(\boldsymbol{x}, \kappa, \Delta t)$ in Eq. (17) depends on the specific system dynamics. It has been proved in Ref. [25] that, for faster system dynamics, Δt should be smaller to ensure a desirable ultimate bound. This also makes sense from a physical point of view that the characteristics of rapidly changing dynamics can only be captured by using a high sampling frequency. For flexible aircraft dynamics, the variations of elastic states are typically faster than the rigid-body states. In Eq. (21), partial derivatives are separately taken with respect to $\boldsymbol{x}_r$, $\boldsymbol{x}_e$, and $\dot{\boldsymbol{x}}_e$. Although the state variation-related terms can all be viewed as perturbations, in which way, the only model information used by the control is $\bar{\boldsymbol{G}}(\boldsymbol{x})$ [Eq. (18)], for relaxing the requirement on the sampling frequency while maintaining the control performance, it is chosen in this paper to include the terms related to the elastic state variations in control design. Nevertheless, because the rigid-body states have slower dynamics, the $\Delta\boldsymbol{x}_r$-related terms are viewed as perturbations by the controller.

The complexity of the control can be further reduced by analyzing the physics of the flexible aircraft. Although the mass matrix of the flexible aircraft is a function of the elastic states, it is still diagonally dominant. Consequently, in the translational and rotational equations, the partial derivatives of the nonlinear coupling terms with respect to $\dot{\boldsymbol{x}}_e$ can become less significant in Δt. Moreover, the partial derivatives of the Coriolis and centrifugal forces with respect to $\boldsymbol{x}_e$ and $\dot{\boldsymbol{x}}_e$ have limited effects on the wing bending dynamics. Therefore, these terms are also viewed as perturbations by the controller. The specific expressions of these partial derivatives can be found in Ref. [38]. For simplicity, the incremental terms in the translational, rotational, bending, and torsion dynamic equations are, respectively, denoted by $\boldsymbol{K}$, $\boldsymbol{W}$, $\boldsymbol{U}$, and $\boldsymbol{Y}$ in Eq. (21). Based on the preceding analyses, in one incremental time step Δt, the $\boldsymbol{K}_r$, $\boldsymbol{W}_r$, $\boldsymbol{U}_r$, and $\boldsymbol{Y}_r$ terms are less influential; thus, they are viewed as perturbations by the controller. The feasibility of this simplification will be verified in Sec. IV.B. Consequently, Eq. (21) is simplified into the following form:

$$
\begin{aligned}
\dot{\boldsymbol{p}}_{V_f} &= \dot{\boldsymbol{p}}_{V_{f_0}} + \left(-\left.\frac{\partial\tilde{\boldsymbol{\omega}}_f\boldsymbol{p}_{V_f}}{\partial\boldsymbol{x}_r}\right|_0\Delta\boldsymbol{x}_r - \left.\frac{\partial\tilde{\boldsymbol{\omega}}_f\boldsymbol{p}_{V_f}}{\partial\dot{\boldsymbol{x}}_e}\right|_0\Delta\dot{\boldsymbol{x}}_e + \left.\frac{\partial\boldsymbol{F}}{\partial\boldsymbol{x}_r}\right|_0\Delta\boldsymbol{x}_r\right) + \left.\frac{\partial\boldsymbol{F}}{\partial\boldsymbol{x}_e}\right|_0\Delta\boldsymbol{x}_e + \left.\frac{\partial\boldsymbol{F}}{\partial\dot{\boldsymbol{x}}_e}\right|_0\Delta\dot{\boldsymbol{x}}_e + \left.\frac{\partial\boldsymbol{F}}{\partial\boldsymbol{u}}\right|_0\Delta\boldsymbol{u} \\
&\triangleq \dot{\boldsymbol{p}}_{V_{f_0}} + \boldsymbol{K}_r + \boldsymbol{K}_e + \boldsymbol{K}_{de} + \boldsymbol{K}_u + \boldsymbol{\epsilon}_1 \\
\dot{\boldsymbol{p}}_{\omega_f} &= \dot{\boldsymbol{p}}_{\omega_{f_0}} + \left(-\left.\frac{\partial\tilde{\boldsymbol{V}}_f\boldsymbol{p}_{V_f} + \tilde{\boldsymbol{\omega}}_f\boldsymbol{p}_{\omega_f}}{\partial\boldsymbol{x}_r}\right|_0\Delta\boldsymbol{x}_r - \left.\frac{\partial\tilde{\boldsymbol{V}}_f\boldsymbol{p}_{V_f} + \tilde{\boldsymbol{\omega}}_f\boldsymbol{p}_{\omega_f}}{\partial\dot{\boldsymbol{x}}_e}\right|_0\Delta\dot{\boldsymbol{x}}_e + \left.\frac{\partial\boldsymbol{M}}{\partial\boldsymbol{x}_r}\right|_0\Delta\boldsymbol{x}_r\right) + \left.\frac{\partial\boldsymbol{M}}{\partial\boldsymbol{x}_e}\right|_0\Delta\boldsymbol{x}_e + \left.\frac{\partial\boldsymbol{M}}{\partial\dot{\boldsymbol{x}}_e}\right|_0\Delta\dot{\boldsymbol{x}}_e + \left.\frac{\partial\boldsymbol{M}}{\partial\boldsymbol{u}}\right|_0\Delta\boldsymbol{u} \\
&\triangleq \dot{\boldsymbol{p}}_{\omega_{f_0}} + \boldsymbol{W}_r + \boldsymbol{W}_e + \boldsymbol{W}_{de} + \boldsymbol{W}_u + \boldsymbol{\epsilon}_2 \\
\dot{\boldsymbol{p}}_{uw} &= \dot{\boldsymbol{p}}_{uw_0} - \mathcal{K}_{uw}\Delta\boldsymbol{q} - \boldsymbol{\mathcal{C}}_{uw}\Delta\boldsymbol{s} + \left(\left.\frac{\partial\boldsymbol{Q}}{\partial\boldsymbol{x}_r}\right|_0\Delta\boldsymbol{x}_r + \left.\frac{\partial(\partial\mathcal{T}/\partial\boldsymbol{q})}{\partial\boldsymbol{x}_r}\right|_0\Delta\boldsymbol{x}_r + \left.\frac{\partial(\partial\mathcal{T}/\partial\boldsymbol{q})}{\partial\boldsymbol{x}_e}\right|_0\Delta\boldsymbol{x}_e + \left.\frac{\partial(\partial\mathcal{T}/\partial\boldsymbol{q})}{\partial\dot{\boldsymbol{x}}_e}\right|_0\Delta\dot{\boldsymbol{x}}_e\right) \\
&\quad + \left.\frac{\partial\boldsymbol{Q}}{\partial\boldsymbol{x}_e}\right|_0\Delta\boldsymbol{x}_e + \left.\frac{\partial\boldsymbol{Q}}{\partial\dot{\boldsymbol{x}}_e}\right|_0\Delta\dot{\boldsymbol{x}}_e + \left.\frac{\partial\boldsymbol{Q}}{\partial\boldsymbol{u}}\right|_0\Delta\boldsymbol{u} \triangleq \dot{\boldsymbol{p}}_{uw_0} + \boldsymbol{U}_q + \boldsymbol{U}_s + \boldsymbol{U}_r + \boldsymbol{U}_e + \boldsymbol{U}_{de} + \boldsymbol{U}_u + \boldsymbol{\epsilon}_3 \\
\dot{\boldsymbol{p}}_{\psi w} &= \dot{\boldsymbol{p}}_{\psi w_0} - \mathcal{K}_{\psi w}\Delta\boldsymbol{\xi} - \boldsymbol{\mathcal{C}}_{\psi w}\Delta\boldsymbol{\eta} + \left.\frac{\partial\boldsymbol{\Theta}}{\partial\boldsymbol{x}_r}\right|_0\Delta\boldsymbol{x}_r + \left.\frac{\partial\boldsymbol{\Theta}}{\partial\boldsymbol{x}_e}\right|_0\Delta\boldsymbol{x}_e + \left.\frac{\partial\boldsymbol{\Theta}}{\partial\dot{\boldsymbol{x}}_e}\right|_0\Delta\dot{\boldsymbol{x}}_e + \left.\frac{\partial\boldsymbol{\Theta}}{\partial\boldsymbol{u}}\right|_0\Delta\boldsymbol{u} \\
&\triangleq \dot{\boldsymbol{p}}_{\psi w_0} + \boldsymbol{Y}_\xi + \boldsymbol{Y}_\eta + \boldsymbol{Y}_r + \boldsymbol{Y}_e + \boldsymbol{Y}_{de} + \boldsymbol{Y}_u + \boldsymbol{\epsilon}_4
\end{aligned}
\tag{21}
$$

$$
\begin{bmatrix} \dot{\boldsymbol{p}}_{V_f} \\ \dot{\boldsymbol{p}}_{\omega_f} \\ \hdashline \dot{\boldsymbol{p}}_{uw} \\ \dot{\boldsymbol{p}}_{\psi w} \\ \hdashline \dot{\boldsymbol{q}} \\ \dot{\boldsymbol{\xi}} \end{bmatrix} = \begin{bmatrix} \dot{\boldsymbol{p}}_{V_{f_0}} \\ \dot{\boldsymbol{p}}_{\omega_{f_0}} \\ \hdashline \dot{\boldsymbol{p}}_{uw_0} \\ \dot{\boldsymbol{p}}_{\psi w_0} \\ \hdashline \dot{\boldsymbol{q}}_0 \\ \dot{\boldsymbol{\xi}}_0 \end{bmatrix} + \left[\begin{array}{c:cc:cc} \boldsymbol{0} & \frac{\partial \boldsymbol{F}}{\partial \boldsymbol{s}} & \frac{\partial \boldsymbol{F}}{\partial \boldsymbol{\eta}} & \frac{\partial \boldsymbol{F}}{\partial \boldsymbol{q}} & \frac{\partial \boldsymbol{F}}{\partial \boldsymbol{\xi}} \\ & \frac{\partial \boldsymbol{M}}{\partial \boldsymbol{s}} & \frac{\partial \boldsymbol{M}}{\partial \boldsymbol{\eta}} & \frac{\partial \boldsymbol{M}}{\partial \boldsymbol{q}} & \frac{\partial \boldsymbol{M}}{\partial \boldsymbol{\xi}} \\ \hdashline \boldsymbol{0} & -\mathcal{C}_{uw} + \frac{\partial \boldsymbol{Q}}{\partial \boldsymbol{s}} & \frac{\partial \boldsymbol{Q}}{\partial \boldsymbol{\eta}} & -\mathcal{K}_{uw} + \frac{\partial \boldsymbol{Q}}{\partial \boldsymbol{q}} & \frac{\partial \boldsymbol{Q}}{\partial \boldsymbol{\xi}} \\ & \frac{\partial \boldsymbol{\Theta}}{\partial \boldsymbol{s}} & -\mathcal{C}_{\psi w} + \frac{\partial \boldsymbol{\Theta}}{\partial \boldsymbol{\eta}} & \frac{\partial \boldsymbol{\Theta}}{\partial \boldsymbol{q}} & -\mathcal{K}_{\psi w} + \frac{\partial \boldsymbol{\Theta}}{\partial \boldsymbol{\xi}} \\ \hdashline \boldsymbol{0} & & \boldsymbol{I} & & \boldsymbol{0} \end{array}\right]_{|0} \begin{bmatrix} \Delta \boldsymbol{V}_f \\ \Delta \boldsymbol{\omega}_f \\ \hdashline \Delta \boldsymbol{s} \\ \Delta \boldsymbol{\eta} \\ \hdashline \Delta \boldsymbol{q} \\ \Delta \boldsymbol{\xi} \end{bmatrix}
$$

$$
+ \left[\begin{array}{cc:cc} \frac{\partial \boldsymbol{F}}{\partial \delta_{a_s}} & \frac{\partial \boldsymbol{F}}{\partial \delta_{a_a}} & \frac{\partial \boldsymbol{F}}{\partial \delta_e} & \frac{\partial \boldsymbol{F}}{\partial \delta_r} \\ \frac{\partial \boldsymbol{M}}{\partial \delta_{a_s}} & \frac{\partial \boldsymbol{M}}{\partial \delta_{a_a}} & \frac{\partial \boldsymbol{M}}{\partial \delta_e} & \frac{\partial \boldsymbol{M}}{\partial \delta_r} \\ \hdashline \frac{\partial \boldsymbol{Q}}{\partial \delta_{a_s}} & \frac{\partial \boldsymbol{Q}}{\partial \delta_{a_a}} & & \\ \frac{\partial \boldsymbol{\Theta}}{\partial \delta_{a_s}} & \frac{\partial \boldsymbol{\Theta}}{\partial \delta_{a_a}} & \multicolumn{2}{c}{\boldsymbol{0}} \\ \hdashline \multicolumn{2}{c:}{\boldsymbol{0}} & \multicolumn{2}{c}{\boldsymbol{0}} \end{array}\right]_{|0} \begin{bmatrix} \Delta \delta_{a_s} \\ \Delta \delta_{a_a} \\ \hdashline \Delta \delta_e \\ \Delta \delta_r \end{bmatrix} + \boldsymbol{\varepsilon} \tag{22}
$$

where $\mathbf{I}$ and $\mathbf{0}$ are the identity matrix and zero matrix. Also, $\boldsymbol{\varepsilon}$ is the augmented perturbation term. In view of Eq. (22), the partial derivatives of the generalized forces with respect to $\boldsymbol{x}_e$ and $\dot{\boldsymbol{x}}_e$ contribute to the aerodynamic stiffness and damping, respectively. Furthermore, the control surface deflections directly lead to acceleration variations.

For the convenience of the virtual control design, define

$$
\boldsymbol{x} = \begin{bmatrix} \boldsymbol{p}_{V_f}^T & \boldsymbol{p}_{\omega_f}^T & \boldsymbol{p}_{uw}^T & \boldsymbol{p}_{\psi w}^T & \boldsymbol{q}^T & \boldsymbol{\xi}^T \end{bmatrix}^T
$$

Velocities and deformations can also be used as states as

$$
\boldsymbol{x}_V = \begin{bmatrix} \boldsymbol{V}_f^T & \boldsymbol{\omega}_f^T & \boldsymbol{s}^T & \boldsymbol{\eta}^T & \boldsymbol{q}^T & \boldsymbol{\xi}^T \end{bmatrix}^T
$$

with a simple transformation of $\boldsymbol{x} = \boldsymbol{M}_s \boldsymbol{x}_V$ and $\boldsymbol{M}_s = \mathrm{diag}([\boldsymbol{M}_{\mathrm{st}}, \mathbf{I}])$. Recalling Eq. (22), the system dynamic equation is represented as

$$
\dot{\boldsymbol{x}} = \dot{\boldsymbol{x}}_0 + \boldsymbol{\Gamma}|_0 \Delta \boldsymbol{x}_V + \boldsymbol{\Upsilon}|_0 \Delta \boldsymbol{u} + \boldsymbol{\varepsilon} \tag{23}
$$

The preceding equation is different from the incremental dynamic equation for rigid aircraft [19,26,27,29] because the $\Delta \boldsymbol{x}_V$-related term still remains:

$$
\Delta \boldsymbol{x}_V \approx \boldsymbol{M}_s^{-1}|_0 \Delta \boldsymbol{x} + \Delta(\boldsymbol{M}_s^{-1}) \boldsymbol{x}_0 + \Delta(\boldsymbol{M}_s^{-1}) \Delta \boldsymbol{x}
$$

where $\Delta(\boldsymbol{M}_s^{-1})$ is caused by the offdiagonal variations of $\Delta \boldsymbol{q}$. Because the mass matrix is diagonally dominant [38], the terms containing $\Delta(\boldsymbol{M}_s^{-1})$ and the higher-order terms can be viewed as perturbations. Note that $\boldsymbol{\varepsilon}'$ is used to combine these terms with the $\boldsymbol{\varepsilon}$ in Eq. (22). Denoting $\boldsymbol{A}_e \triangleq (\boldsymbol{\Gamma} \boldsymbol{M}_s^{-1})|_0$ and $\boldsymbol{B}_e \triangleq \boldsymbol{\Upsilon}|_0$, Eq. (22) is then simplified to

$$
\dot{\boldsymbol{x}} = \dot{\boldsymbol{x}}_0 + \boldsymbol{A}_e \Delta \boldsymbol{x} + \boldsymbol{B}_e \Delta \boldsymbol{u} + \boldsymbol{\varepsilon}' \tag{24}
$$

The main control aim of this paper is load alleviation, and so a reference model is designed to generate references for the states and state derivatives for load control purposes. The internal loads, also known as "stress resultants", are caused by the externally applied forces and moments. The strategy of this controller is to use control surface deflections to compensate for the load variations caused by perturbations so that the generalized forces are retained at their nominal values of $\boldsymbol{F}_*$, $\boldsymbol{M}_*$, $\boldsymbol{Q}_*$ and $\boldsymbol{\Theta}_*$. The subscript $*$ indicates the nominal trimmed condition. Expanding the total force as the nominal force $\boldsymbol{F}_*$, the force's variations due to aerodynamic uncertainties $\Delta \boldsymbol{F}_a$, caused by atmospheric disturbances $\Delta \boldsymbol{F}_d$, and generated by control inputs $\Delta \boldsymbol{F}_c$ are shown as

$$
\boldsymbol{F} = \boldsymbol{F}_* + \Delta \boldsymbol{F}_a + \Delta \boldsymbol{F}_d + \Delta \boldsymbol{F}_c \tag{25}
$$

The moment $\boldsymbol{M}$ and the generalized elastic forces $\boldsymbol{Q}$ and $\boldsymbol{\Theta}$ in Eq. (3) can also be expanded in this form. To retain the forces and moments at their nominal values, the desired forces generated by the control surfaces should be

$$
\begin{aligned} \Delta \boldsymbol{F}_c &= -\Delta(\boldsymbol{F}_a + \boldsymbol{F}_d), \quad \Delta \boldsymbol{M}_c = -\Delta(\boldsymbol{M}_a + \boldsymbol{M}_d) \\ \Delta \boldsymbol{Q}_c &= -\Delta(\boldsymbol{Q}_a + \boldsymbol{Q}_d), \quad \Delta \boldsymbol{\Theta}_c = -\Delta(\boldsymbol{\Theta}_a + \boldsymbol{\Theta}_d) \end{aligned} \tag{26}
$$

Recalling Eq. (3), in order to satisfy the preceding equations, assuming the Coriolis and centrifugal forces are small, the virtual control

$$
\boldsymbol{\nu}_{rm} = \begin{bmatrix} \boldsymbol{\nu}_{P_{V_f}}^T & \boldsymbol{\nu}_{P_{\omega f}}^T & \boldsymbol{\nu}_{P_{uw}}^T & \boldsymbol{\nu}_{P_{\psi w}}^T & \boldsymbol{\nu}_q^T & \boldsymbol{\nu}_\xi^T \end{bmatrix}^T
$$

can be designed as

$$
\begin{aligned} \boldsymbol{\nu}_{P_{V_f}} &= -\tilde{\boldsymbol{\omega}}_f \boldsymbol{p}_{V_f} + \boldsymbol{F}_* \\ \boldsymbol{\nu}_{P_{\omega_f}} &= -\tilde{\boldsymbol{V}}_f \boldsymbol{p}_{V_f} - \tilde{\boldsymbol{\omega}}_f \boldsymbol{p}_{\omega_f} + \boldsymbol{M}_* \\ \boldsymbol{\nu}_{P_{uw}} &= -\mathcal{K}_{uw} \boldsymbol{q} - \mathcal{C}_{uw} \boldsymbol{s} + \boldsymbol{Q}_* = -\mathcal{K}_{uw}(\boldsymbol{q} - \boldsymbol{q}_*) - \mathcal{C}_{uw}(\boldsymbol{s} - \boldsymbol{s}_*) \\ \boldsymbol{\nu}_{P_{\psi w}} &= -\mathcal{K}_{\psi w} \boldsymbol{\xi} - \mathcal{C}_{\psi w} \boldsymbol{\eta} + \boldsymbol{\Theta}_* = -\mathcal{K}_{\psi w}(\boldsymbol{\xi} - \boldsymbol{\xi}_*) - \mathcal{C}_{\psi w}(\boldsymbol{\eta} - \boldsymbol{\eta}_*) \\ \boldsymbol{\nu}_q &= \boldsymbol{0}, \boldsymbol{\nu}_\xi = \boldsymbol{0} \end{aligned} \tag{27}
$$

If the nominal condition is steady level flight, then $\boldsymbol{F}_* = \boldsymbol{M}_* = \boldsymbol{s}_* = \boldsymbol{\eta}_* = \boldsymbol{0}$. The nominal condition can also be constant speed climb and decent, level turn, etc. The desired $\dot{\boldsymbol{q}}$ and $\dot{\boldsymbol{\xi}}$ are all equal to zero. The references for states are obtained by integrating the virtual control as

$$
\boldsymbol{x}_{rm} = \boldsymbol{x}_{rm_*} + \int_0^t \boldsymbol{\nu}_{rm} \mathrm{d}\tau \tag{28}
$$

A proportional virtual control term $\boldsymbol{\nu}_p$ is added to minimize the reference tracking errors as

$$
\boldsymbol{\nu} = \boldsymbol{\nu}_{rm} + \boldsymbol{\nu}_p = \boldsymbol{\nu}_{rm} + \boldsymbol{K}_p(\boldsymbol{x}_{rm} - \boldsymbol{x}) \tag{29}
$$

where $\boldsymbol{K}_p$ is a positive definite gain matrix (the same as in Proposition 2). Using Eq. (24), and based on Sec. III.A, the INDI GLA control law is designed as follows:

$$
\Delta \boldsymbol{u} = (\boldsymbol{B}_e^T \boldsymbol{W} \boldsymbol{B}_e)^{-1} \boldsymbol{B}_e^T \boldsymbol{W}(\boldsymbol{\nu} - \dot{\boldsymbol{x}}_0 - \boldsymbol{A}_e \Delta \boldsymbol{x}) \tag{30}
$$

For the reason that the number of control variables is less than the number of states, the weighted least-squares method is used in the present INDI control law. The weighting matrix $\boldsymbol{W}$ is chosen as a

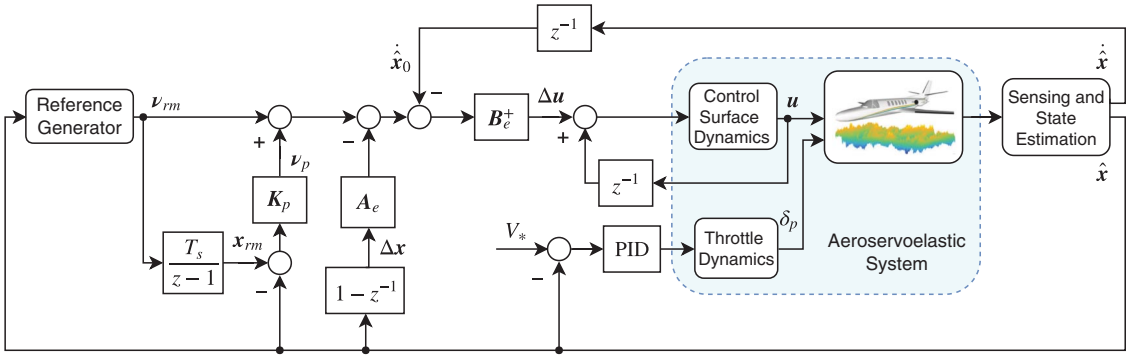

Fig. 5 Flexible aircraft INDI gust load alleviation control law structure.

positive definite matrix, which can be tuned based on the control priority. The total control command for the actuator is $\boldsymbol{u} = \Delta\boldsymbol{u} + \boldsymbol{u}_0$, where $\boldsymbol{u}_0$ is the sampled actuator position vector [25]. A block diagram is illustrated in Fig. 5, in which z^{-1} represents one time-step delay, $T_s/(z-1)$ is a discretized integrator using the forward Euler method, and PID represents a proportional–integral–derivative regulator.

C. Sensing and State Estimation

The INDI GLA control law given by Eqs. (27) and (30) requires the feedback of the states and state derivatives. The rigid-body states $\boldsymbol{x}_r = [\boldsymbol{V}_f^T \quad \boldsymbol{\omega}_f^T]^T$ and $\dot{\boldsymbol{V}}_f$ can be obtained from the integrated inertial navigation system. Angular accelerations can be directly measured by angular accelerometers [39], numerically differentiated from gyroscope measurements [22], predicted by a linear predictive filter [19], etc.

The elastic states $\boldsymbol{x}_e = \boldsymbol{H}[\boldsymbol{q}^T \quad \boldsymbol{\xi}^T]^T$ can be estimated using an online observer. In this paper, the bending and torsion motions are captured by nine accelerometers on the flexible aircraft. As shown by the red dots in Fig. 1, one accelerometer is installed on the center of mass and eight accelerometers are placed on the wings. On each wing, the accelerometers are placed in pairs at the midspan and the wing tip. For each pair, one accelerometer is placed in front of the elastic axis, and the other one is behind, such that the torsional deformations can be observed. The accelerometers on the wing are placed along with the z axis of the local wing coordinate (Fig. 1).

Consider an infinitesimal mass element dm on the wing, for which the absolute velocities are given as [38]

$$\bar{\boldsymbol{v}}_w(\boldsymbol{r}_w, t) = \boldsymbol{C}_w\boldsymbol{V}_f + \boldsymbol{C}_w\tilde{\boldsymbol{r}}_{fw}^T\boldsymbol{\omega}_f + \left(\tilde{\boldsymbol{r}}_w + \widetilde{\boldsymbol{\Phi}\boldsymbol{q}}\right)^T\boldsymbol{C}_w\boldsymbol{\omega}_f + \tilde{\boldsymbol{r}}_w^T\boldsymbol{\Psi}\boldsymbol{\eta} + \boldsymbol{\Phi}\boldsymbol{s} \tag{31}$$

By differentiating Eq. (31), the acceleration vector of the infinitesimal mass element is

$$\begin{aligned}\boldsymbol{a}_w(\boldsymbol{r}_w, t) = {} & \boldsymbol{C}_w\dot{\boldsymbol{V}}_f + \boldsymbol{C}_w\tilde{\boldsymbol{r}}_{fw}^T\dot{\boldsymbol{\omega}}_f + \left(\tilde{\boldsymbol{r}}_w + \widetilde{\boldsymbol{\Phi}\boldsymbol{q}}\right)^T\boldsymbol{C}_w\dot{\boldsymbol{\omega}}_f \\ & + \widetilde{\boldsymbol{\Phi}\boldsymbol{s}}^T\boldsymbol{C}_w\boldsymbol{\omega}_f + \tilde{\boldsymbol{r}}_w^T\Psi\dot{\boldsymbol{\eta}} + \boldsymbol{\Phi}\dot{\boldsymbol{s}}\end{aligned} \tag{32}$$

Evaluating $\boldsymbol{r}_w$ in Eq. (32) by the position vector of a wing accelerometer then, theoretically, its measurement is given by the z component of $\boldsymbol{a}_w(\boldsymbol{r}_w, t)$. In reality, the measurements always contain noise $\boldsymbol{v}$. Therefore, the system output equation is written as $\boldsymbol{y} = \boldsymbol{h}(\boldsymbol{x}) + \boldsymbol{v}$, where $\boldsymbol{h}(\boldsymbol{x})$ is based on Eq. (32).

The extended Kalman filter and unscented Kalman filter are widely used for the state estimation of nonlinear systems. However, these two methods require high computational power. Because the nonlinear INDI control is able to retain the states near the equilibrium point, the linear Kalman filter is a reasonable and efficient observer for systems under INDI control. It is noteworthy that the accelerometer measurements are calculated using the full-order nonlinear flexible aircraft model, whereas only the reduced-order model is available for the observer design. Linearizing the reduced-order model around the equilibrium point, the resulting dynamics are written as

$$\begin{bmatrix}\dot{\boldsymbol{x}}_r \\ \ddot{\boldsymbol{x}}_e \\ \dot{\boldsymbol{x}}_e\end{bmatrix} = \begin{bmatrix}\boldsymbol{A}_{rr} & \boldsymbol{A}_{re} \\ \boldsymbol{A}_{er} & \boldsymbol{A}_{ee}\end{bmatrix}\begin{bmatrix}\boldsymbol{x}_r \\ \dot{\boldsymbol{x}}_e \\ \boldsymbol{x}_e\end{bmatrix} + \begin{bmatrix}\boldsymbol{B}_r \\ \boldsymbol{B}_{el}\end{bmatrix}\boldsymbol{u} + \begin{bmatrix}\boldsymbol{w}_r \\ \boldsymbol{w}_e\end{bmatrix}$$
$$\boldsymbol{y}_V = \begin{bmatrix}\boldsymbol{C}_r & \boldsymbol{C}_{el}\end{bmatrix}\begin{bmatrix}\boldsymbol{x}_r & \dot{\boldsymbol{x}}_e & \boldsymbol{x}_e\end{bmatrix}^T + \boldsymbol{D}_V\boldsymbol{u} + \boldsymbol{v} \tag{33}$$

The process noise $[\boldsymbol{w}_r^T \quad \boldsymbol{w}_e^T]^T$ contains the model errors and external disturbances. For GLA problems, it is common to augment the linear system models with the Dryden turbulence model as a prior knowledge of the process noise [10,40]. In reality, however, the turbulence spectrum is usually unknown. To get a satisfactory state estimation while making the controller capable of handling a broad range of disturbances, the Dryden model is augmented into the system model with parametric uncertainties. These uncertain parameters can be modeled as random walks and be estimated online. Recalling Eq. (12), the state-space realization of the Dryden spectrum can be given by

$$\begin{aligned}\dot{\boldsymbol{x}}_w &= \boldsymbol{A}_g\boldsymbol{x}_w + \boldsymbol{B}_g\boldsymbol{n} \\ \boldsymbol{w}_{g_w} &= \boldsymbol{C}_g\boldsymbol{x}_w\end{aligned} \tag{34}$$

where $\boldsymbol{n}$ is the Gaussian white noise. In view of Fig. 3, the gust velocity varies on each strip. However, for maintaining the observation efficiency, the gust velocities are assumed to be uniformly distributed on the wing $\boldsymbol{w}_{g_w}$ and the tail $\boldsymbol{w}_{g_H}$ in the observation process. Also, the gust penetration effect is roughly modeled as a time shift ς from the wing to the tail in the observation process. In other words, the current gust velocities on the tail equal the gust velocities on the wing ς seconds ago, i.e., $\boldsymbol{w}_{g_H} = e^{-\varsigma s}\boldsymbol{w}_{g_w}$. The pure time delay $e^{-\varsigma s}$ is approximated using the fifth-order Padé approximation in the Laplace domain, which can be realized in the time domain as

$$\begin{aligned}\boldsymbol{w}_{g_H} &= e^{-\varsigma s}\boldsymbol{w}_{g_w} \approx H(\varsigma s)\boldsymbol{w}_{g_w} \\ \dot{\boldsymbol{x}}_\varsigma &= \boldsymbol{A}_\varsigma\boldsymbol{x}_\varsigma + \boldsymbol{B}_\varsigma\boldsymbol{w}_{g_w} = \boldsymbol{A}_\varsigma\boldsymbol{x}_\varsigma + \boldsymbol{B}_\varsigma\boldsymbol{C}_g\boldsymbol{x}_w, \quad \boldsymbol{w}_{g_H} = \boldsymbol{C}_\varsigma\boldsymbol{x}_\varsigma\end{aligned} \tag{35}$$

The influences of gust on the elastic modes are modeled as $\boldsymbol{w}_e = \boldsymbol{E}_w\boldsymbol{w}_{g_w} + \boldsymbol{E}_H\boldsymbol{w}_{g_H} + \boldsymbol{d}_e$, with $\boldsymbol{d}_e$ representing the aircraft and turbulence model errors. Because the rigid states $\boldsymbol{x}_r$ can be directly measured, they are treated as inputs to the elastic state estimation equation. In summary, the integrated linear model for Kalman filter estimation is written as

$$\begin{bmatrix} \ddot{\boldsymbol{x}}_e \\ \dot{\boldsymbol{x}}_e \\ \hdashline \dot{\boldsymbol{x}}_w \\ \dot{\boldsymbol{x}}_\varsigma \end{bmatrix} = \left[\begin{array}{c:cc} \boldsymbol{A}_{ee} & \boldsymbol{E}_w\boldsymbol{C}_g & \boldsymbol{E}_H\boldsymbol{C}_\varsigma \\ \hdashline \boldsymbol{0} & \boldsymbol{A}_g & \boldsymbol{0} \\ \boldsymbol{0} & \boldsymbol{B}_\varsigma\boldsymbol{C}_g & \boldsymbol{A}_\varsigma \end{array}\right] \begin{bmatrix} \dot{\boldsymbol{x}}_e \\ \boldsymbol{x}_e \\ \hdashline \boldsymbol{x}_w \\ \boldsymbol{x}_\varsigma \end{bmatrix} + \left[\begin{array}{c:c} \boldsymbol{B}_{el} & \boldsymbol{A}_{er} \\ \hdashline \boldsymbol{0} & \boldsymbol{0} \\ \boldsymbol{0} & \boldsymbol{0} \end{array}\right] \begin{bmatrix} \boldsymbol{u} \\ \hdashline \boldsymbol{x}_r \end{bmatrix} + \begin{bmatrix} \boldsymbol{0} \\ \hdashline \boldsymbol{B}_g \\ \boldsymbol{0} \end{bmatrix} \boldsymbol{n} + \begin{bmatrix} \boldsymbol{d}_e \\ \hdashline \boldsymbol{0} \\ \boldsymbol{0} \end{bmatrix}$$

$$\boldsymbol{y}_V = \left[\begin{array}{c:cc} \boldsymbol{C}_{el} & \boldsymbol{0} & \boldsymbol{0} \end{array}\right] \left[\begin{array}{c:cc} \dot{\boldsymbol{x}}_e & \boldsymbol{x}_e & \boldsymbol{x}_w \quad \boldsymbol{x}_\varsigma \end{array}\right]^T + \left[\begin{array}{c:c} \boldsymbol{D}_V & \boldsymbol{C}_r \end{array}\right] \left[\begin{array}{c:c} \boldsymbol{u} & \boldsymbol{x}_r \end{array}\right]^T + \boldsymbol{v} \tag{36}$$

which is written in a more compact form as

$$\begin{aligned} \dot{\boldsymbol{x}}_{kf} &= \boldsymbol{A}_{kf}\boldsymbol{x}_{kf} + \boldsymbol{B}_{kf}\boldsymbol{u}_{kf} + \boldsymbol{G}_{kf}\boldsymbol{n} + \boldsymbol{d}_{kf} \\ \boldsymbol{y}_{kf} &= \boldsymbol{C}_{kf}\boldsymbol{x}_{kf} + \boldsymbol{D}_{kf}\boldsymbol{u}_{kf} + \boldsymbol{v} \end{aligned} \tag{37}$$

The measurement noise covariance matrix is $\boldsymbol{R}_{kf} = E\{\boldsymbol{v}\boldsymbol{v}^T\}$, which is set based on the realistic noise level of the sensors. The process noise covariance matrix is chosen as $\boldsymbol{Q}_{kf} = E\{\boldsymbol{G}_{kf}\boldsymbol{n}\boldsymbol{n}^T\boldsymbol{G}_{kf}^T\} + \boldsymbol{Q}_d$, where $\boldsymbol{Q}_d$ is an additive matrix tuned to account for the aircraft and turbulence model errors. The effectiveness of this state estimation approach will be shown in Sec. IV.C.

IV. Simulation Results and Discussions

The effectiveness of the proposed controller on gust load alleviation and its robustness to model uncertainties and actuator faults will be evaluated in this section. A nonlinear full-order benchmark flexible aircraft validation model is set up using the geometry, inertia, and stiffness data published in Ref. [2]. The dynamics of this aircraft have been discussed in Sec. II. Each side of the wing model contains five bending modes and five torsion modes. The eigenfunctions of a uniform cantilever beam and a uniform clamped–free shaft are used as the bending shape functions $\Phi(\boldsymbol{r}_w)$ and the torsion shape functions $\Psi(\boldsymbol{r}_w)$, respectively. The rest of the aircraft components are assumed to be rigid. Different from the quasi-steady strip theory used in Ref. [2], a modified strip theory (Sec. II.B) is adopted in this paper. This validation model uses the steady-flow lift curve slope [$C_{L_\alpha}^{\mathrm{SF}}$ in Eq. (5)] provided by Ref. [2]. These values are corrected using the Prandtl-Glauert factor to consider compressibility. The distributed forces on the right and left lifting surfaces are calculated independently; in which way, the lateral flight dynamic modes can be considered.

All the control surface actuator dynamics are modeled as first-order systems with time constants of 0.02 s. The deflection limits of ailerons, elevators, and rudders are ±30 deg, ±20 deg, and ±20 deg respectively. The rate limits for ailerons are 100 deg/s, and they are 60 deg/s for the elevator and rudder. The sampling frequency is $f_s = 1000$ Hz for capturing the high-frequency elastic modes. For the load cases considered in this paper, the variations of the airspeed are within ±0.2 m/s in the open-loop responses, and thus constant throttle is assumed in the subsequent simulations. A simple proportional–integral–derivative throttle controller can always be used if the airspeed has large deviations.

A. Trim and Model Analysis

To analyze the couplings between the structural and rigid-body dynamics, a quasi-rigid aircraft model [2,29] is set up. This quasi-rigid aircraft assumes infinitely high wing stiffness, and its kinematic equations are equal to Eq. (1). The dynamics of this quasi-rigid aircraft is described by the first two equations of Eq. (3), and all the elastic motion-related terms are set to zero. The resulting six-degree-of-freedom equations become identical to the conventional rigid aircraft dynamic equations expressed in the body-fixed frame when O_f coincides with the center of mass. Quasi-steady aerodynamics are used by this quasi-rigid aircraft model.

The full-order flexible aircraft model contains 20 elastic modes (10 for each wing) and 97 aerodynamic strips; thus, referring to Sec. III.B, the total number of states equals 440. As presented in Sec. III.B, a reduced-order nonlinear flexible aircraft model is used for control design. This model only includes the first three structural modes on each wing, coupled with quasi-steady aerodynamics; thus, the total number of states is reduced to 24. The unsteady aerodynamic effects are viewed as perturbations to the controller (Sec. III.B). The control designed using the reduced-order model will be implemented on the full-order model to evaluate its effectiveness.

Using the distributed inertia and stiffness data in Ref. [2], the natural frequency of the first wing elastic mode is 36.4 rad/s, which may not be representative for a very flexible aircraft. To evaluate the genericity of the proposed controller, a more flexible aircraft model is set up, which reduces the bending and torsion stiffness of the benchmark flexible aircraft model by 80%. Consequently, the natural frequency of the first wing elastic mode becomes 16.34 rad/s (2.6 Hz). The structural damping matrices $\boldsymbol{\mathcal{C}}_{uw}$ and $\boldsymbol{\mathcal{C}}_{ww}$ are assumed to be proportional to the stiffness matrices in Ref. [2]. Therefore, these damping matrices are also reduced by 80% in this more flexible aircraft model.

The quasi-rigid aircraft, the full-order benchmark flexible aircraft, the reduced-order flexible aircraft, and the flexible aircraft with 80% reduced stiffness are all trimmed at a steady level flight condition, with $h_* = 25{,}000$ ft, $V_{E_*} = 127$ m/s, and $M_{a_*} = 0.41$. The steady level flight trim constraints are given by

$$\begin{aligned} &\dot{\boldsymbol{R}}_{f_*} = [V_{E_*} \quad 0 \quad 0]^T, \quad \boldsymbol{\theta}_{f_*} = [0 \quad \theta_* \quad 0]^T, \quad \boldsymbol{V}_{f_*} = \boldsymbol{C}_f(\boldsymbol{\theta}_*)\dot{\boldsymbol{R}}_{f_*}, \\ &\boldsymbol{\omega}_{f_*} = \boldsymbol{0}, \quad \alpha_* = \theta_*, \quad \beta_* = 0, \quad \boldsymbol{s}_* = \boldsymbol{0}, \quad \boldsymbol{\eta}_* = \boldsymbol{0} \end{aligned} \tag{38}$$

In view of the symmetric characteristic of the steady level flight condition, asymmetric states and control inputs are automatically set to be zero. The trim solutions for the considered flight condition satisfying Eq. (38) are summarized in Table 1.

F_{E_*} and δ_{e_*} in Table 1, respectively, represent the thrust and elevator deflections in the trim condition. For the present models, the wing elastic axis coincides with the unswept wing beam; thus, the bending and torsion modes are decoupled. Also, the aerodynamic center of the wing is in front of the elastic axis. Consequently, in the trim condition, the wing is bending upward with a noseup torsional angle. Because of this noseup twist, α_* of the flexible aircraft are smaller than that of the quasi-rigid aircraft. The trim solutions of the

Table 1 Trim solutions for four aircraft models

	α_*, deg	δ_{e_*}, deg	F_{E_*}, N	$\boldsymbol{q}_*$, mm	$\boldsymbol{\xi}_*$, deg
Quasi rigid	4.03	−3.71	2809	— —	— —
Full-order flexible	3.98	−3.61	2782	$[-34.96, 4.36, -0.36, 0.01, -0.03]^T$	$[0.114, -0.020, 0.008, -0.003, 0.002]^T$
Reduced-order flexible	3.98	−3.61	2782	$[-34.29, 3.63]^T$	0.114
Full-order flexible with reduced stiffness	3.76	−3.23	2675	$[-183.41, 23.57, -2.03, 0.07, -0.14]^T$	$[0.588, -0.111, 0.043, -0.014, 0.009]^T$

reduced-order and full-order flexible aircraft are close to each other. Moreover, the flexible aircraft with reduced stiffness has larger deformations than the benchmark flexible aircraft, which can be seen from the values of $\boldsymbol{q}_*$ and $\boldsymbol{\xi}_*$ in Table 1.

An eigenvalue analysis is performed to show the characteristics of the four models. Figure 6 compares the poles of the quasi-rigid aircraft and two flexible aircraft. Due to the coupling effects, the rigid mode poles of the flexible aircraft deviate from the poles of the quasi-rigid aircraft. For all the models, there are four poles in the origin for X_E, Y_E, Z_E, and ψ. The reduced-order model is able to maintain the low–frequency characteristics of the full-order system. As can be seen from Fig. 6, the poles of the reduced-order model are in agreement with that of the full-order model in the low-frequency range. The distinctions between these two models increase as the frequency increases.

Figure 7 compares the poles of the quasi-rigid, the benchmark flexible, and the flexible aircraft with reduced stiffness. It can be observed that the elastic modes of the flexible aircraft with 80% reduced stiffness have reduced frequency and a higher damping ratio. For example, as the stiffness reduces, the first bending mode frequency reduces from 42.5 to 23.1 rad/s, whereas the damping ratio increases from 0.101 to 0.153. Besides, the frequency of the first torsion mode reduces from 263 to 115 rad/s, whereas the damping ratio increases from 0.029 to 0.033. As the wing flexibility increases, the couplings between the structural and rigid-body dynamics become more prominent. In view of the third subplot of Fig. 7, the benchmark full-order flexible aircraft has a higher short-period damping ratio than the quasi-rigid aircraft, which coincides with the results in Refs. [41,42]. When 80% of the wing stiffness is reduced, the pair of complex conjugate short-period poles merges to become two real poles. The disappearance of the conventional oscillatory short-period mode caused by the wing flexibility was also reported in Refs. [5,43,44]. The dominant pitching pole of the more flexible aircraft is -0.783, which is expected to move to the unstable region as the wing stiffness further reduces [44]. The reduction of wing stiffness also induces an unstable phugoid mode, which is observed from the fourth subplot of Fig. 7. This phenomenon is in agreement with the results in Refs. [5,43,45]. In addition, the lateral flight dynamic modes are also influenced by the wing flexibility. These couplings between the rigid-body and structural dynamics highlight the necessity of an integrated controller, which can simultaneously consider the aeroelastic and flight dynamic control objectives.

B. Validation of the Model Simplification

According to the analysis in Sec. III.B, the $\boldsymbol{K}_r$, $\boldsymbol{W}_r$, $\boldsymbol{U}_r$, and $\boldsymbol{Y}_r$ terms in Eq. (21) are less influential in one incremental time step; thus, they are viewed as perturbations by the controller. To validate this process, the values of the terms in Eq. (21) will be numerically compared in this subsection.

The benchmark flexible aircraft is initially trimmed in a steady level flight condition. The 1 deg step elevator δ_e, rudder δ_r, symmetric δ_{a_s}, and asymmetric δ_{a_a} aileron deflection commands are separately given to the aircraft. In one incremental time step of $\Delta t = 0.001$ s, the norm values of the terms in Eq. (21) are shown in Fig. 8. For clarity, only the terms in the translational, rotational, and right wing vibration equations are shown in the figure. The left wing vibrations are exactly symmetrical or asymmetrical to the right wing.

It can be seen from Fig. 8 that the elevator (δ_e blue circles) and rudder (δ_r red cross) deflections directly lead to translational and

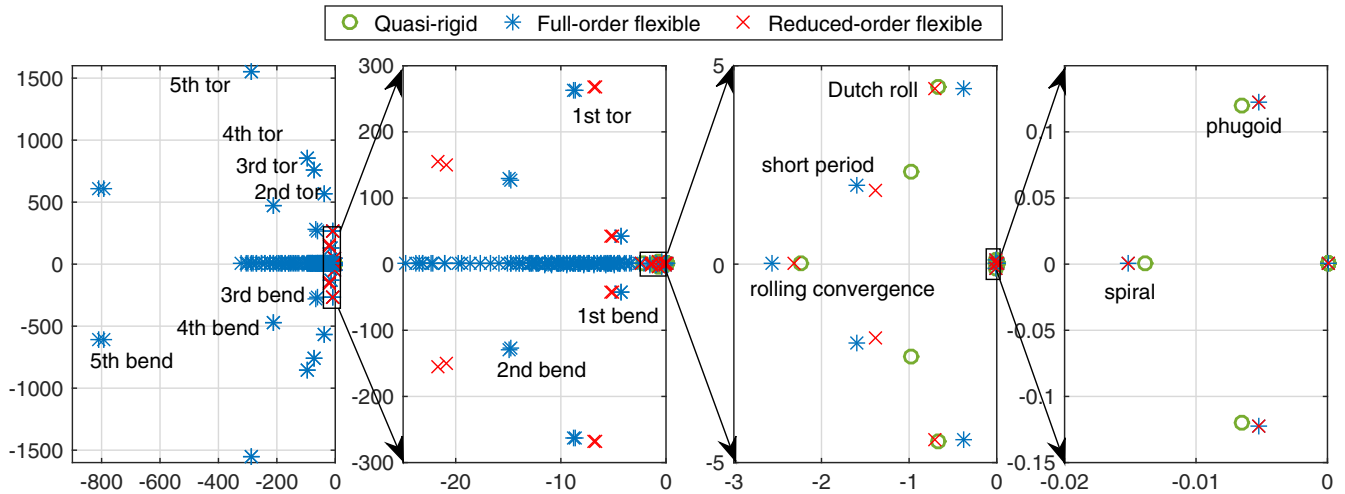

Fig. 6 Eigenvalues of the quasi-rigid, full-, and reduced-order flexible aircraft models (tor denotes torsion, and bend denotes bending).

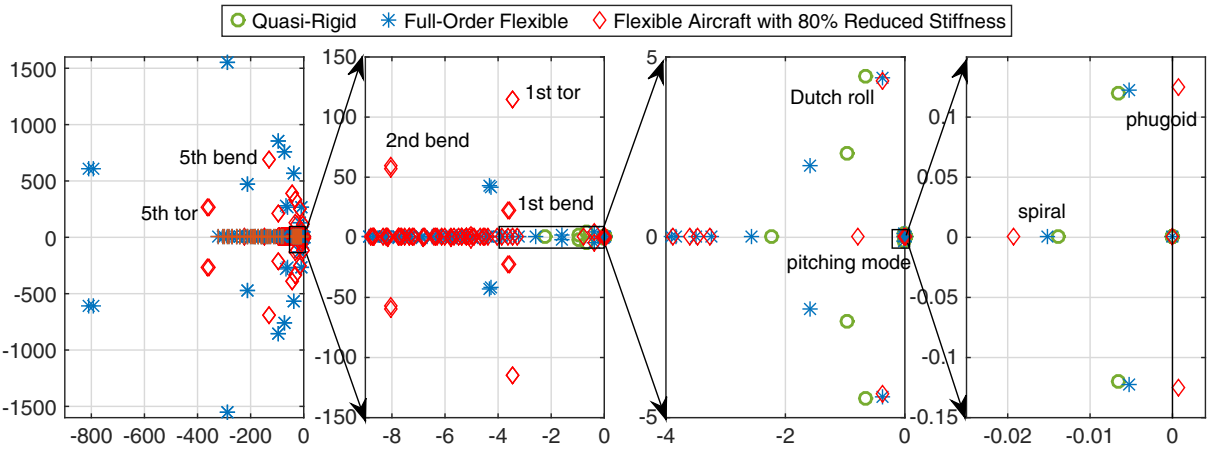

Fig. 7 Eigenvalues of the quasi-rigid and full-order flexible aircraft, as well as a flexible aircraft with 80% reduced stiffness.

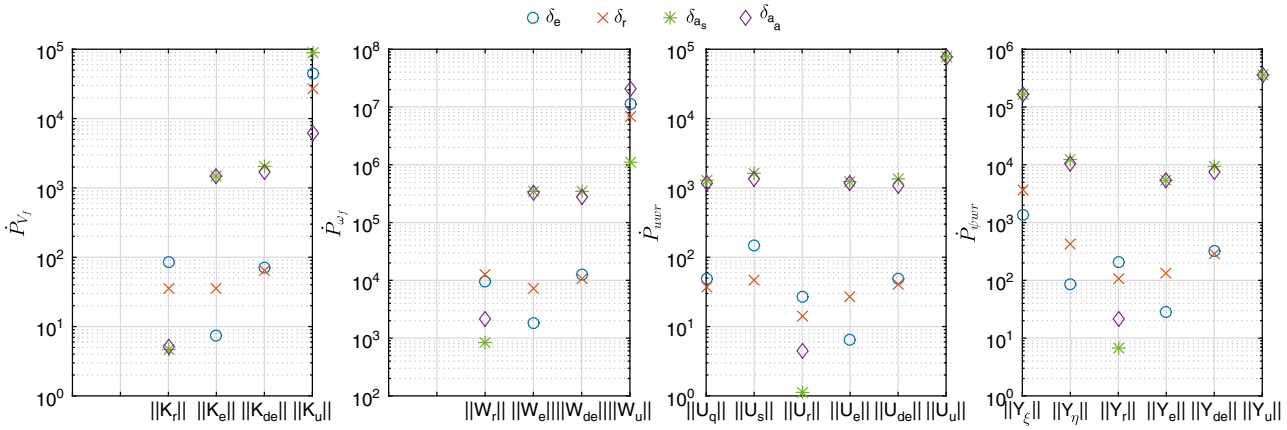

Fig. 8 Norm value of the terms in Eq. (21) in one incremental time step.

rotational acceleration variations because $\|\boldsymbol{K}_u\|$ and $\|\boldsymbol{W}_u\|$ are at least two orders of magnitude larger than $\|\boldsymbol{K}_r\|$, $\|\boldsymbol{K}_e\|$, $\|\boldsymbol{K}_{de}\|$, $\|\boldsymbol{W}_r\|$, $\|\boldsymbol{W}_e\|$, and $\|\boldsymbol{W}_{de}\|$. Also, δ_e and δ_a do not directly influence the generalized elastic forces $\boldsymbol{Q}$ and $\boldsymbol{\Theta}$, thus $\|\boldsymbol{U}_u\| = \|\boldsymbol{Y}_u\| = 0$. Even so, the elevator and rudder deflections indirectly excite bending and torsion motions due to the coupling effects because $\|\boldsymbol{U}_q\|$, $\|\boldsymbol{U}_s\|$, $\|\boldsymbol{U}_r\|$, $\|\boldsymbol{U}_e\|$, $\|\boldsymbol{U}_{de}\|$, $\|\boldsymbol{Y}_\xi\|$, $\|\boldsymbol{Y}_\eta\|$, $\|\boldsymbol{Y}_r\|$, $\|\boldsymbol{Y}_e\|$, and $\|\boldsymbol{Y}_{de}\|$ are nonzero.

The symmetric aileron (δ_{a_s} green asterisks) deflections directly lead to translational $\|\boldsymbol{K}_u\|$, bending $\|\boldsymbol{U}_u\|$, and torsion $\|\boldsymbol{Y}_u\|$ accelerations, as well as small pitching accelerations $\|\boldsymbol{W}_u\|$. The $\boldsymbol{u}$-related terms are about 40, 4, and 40 times larger than the $\boldsymbol{x}_e$- and $\dot{\boldsymbol{x}}_e$-related terms in the translational, rotational, and bending equations, respectively. $\|\boldsymbol{Y}_\xi\|$ is comparable with $\|\boldsymbol{Y}_u\|$ because the wing torsion modes have a higher frequency and a smaller damping ratio than the bending modes (Fig. 6). Nevertheless, under δ_{a_s} deflections, $\|\boldsymbol{K}_r\|$, $\|\boldsymbol{W}_r\|$, $\|\boldsymbol{U}_r\|$, and $\|\boldsymbol{Y}_r\|$ are at least two orders of magnitude smaller than the remaining terms.

The term values under the asymmetric aileron (δ_{a_a}; purple diamonds) excitation show similar phenomena as under δ_{a_s} excitation. Namely, the $\boldsymbol{x}_e$- and $\dot{\boldsymbol{x}}_e$-related terms have comparable variations as compared to the $\boldsymbol{u}$ related terms, whereas $\|\boldsymbol{K}_r\|$, $\|\boldsymbol{W}_r\|$, $\|\boldsymbol{U}_r\|$, and $\|\boldsymbol{Y}_r\|$ are at least two orders of magnitude smaller than the remaining terms. The simulation results in this subsection further verify the feasibility of viewing $\boldsymbol{K}_r$, $\boldsymbol{W}_r$, $\boldsymbol{U}_r$, and $\boldsymbol{Y}_r$ as perturbations in the control design process (Sec. III.B).

C. State Estimation Results and Discussions

The method presented in Sec. III.C will be used to estimate the elastic states $\boldsymbol{x}_e$ and $\dot{\boldsymbol{x}}_e$ while the flexible aircraft fly through a 2-D von Kármán turbulence field (Fig. 3). The parameters of the turbulence field are $L_g = 762$ m and $\sigma = 1.5$ m/s. The measurement noise $\boldsymbol{v}$ is modeled as white noise with a standard deviation of 0.03 m/s^2. The turbulence parameters used by the Dryden model are $L_g = 800$ m and $\sigma = 1.8$ m/s, which are chosen to be different from the actual turbulence field for including the parametric uncertainties. As mentioned in Sec. III.C, these uncertain parameters can be modeled as a random walk and be estimated online. In this research, by tuning the process noise covariance matrix $\boldsymbol{Q}_{kf}$, the Kalman filter already shows satisfactory results without directly estimating these uncertain parameters.

Figure 9 illustrates the real and estimated deformation velocities of the first and second bending modes, as well as the first torsion mode. As can be seen from Figs. 9 and 10, the Kalman filter online estimation converges within 0.02 s. The estimation errors are all within the posterior estimate standard deviation boundary.

The deformation accelerations $\ddot{\boldsymbol{x}}_e$ can be reconstructed from linear accelerometer measurements. As an alternative, $\ddot{\boldsymbol{x}}_e$ can also be obtained by passing $\dot{\boldsymbol{x}}_e$ through a "washout" filter: $s\omega_n^2/(s^2 + 2\zeta_n\omega_n s + \omega_n^2)$. The estimation results of the deformation accelerations are shown in Fig. 11, in which only small disagreements between the real and estimated values present.

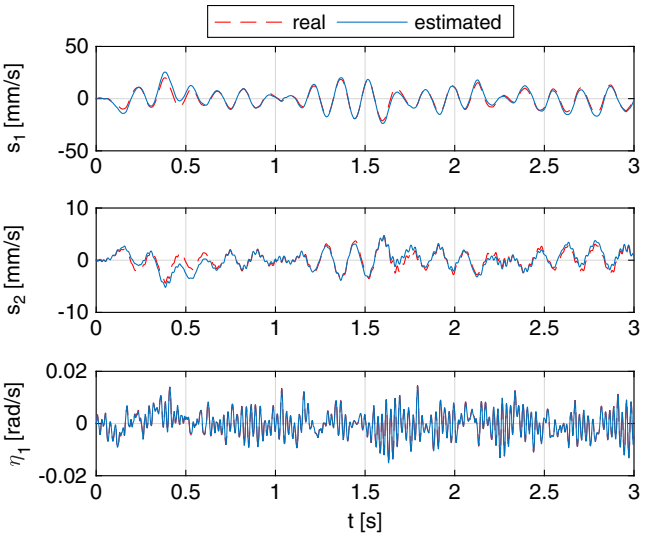

Fig. 9 Real and estimated deformation velocities.

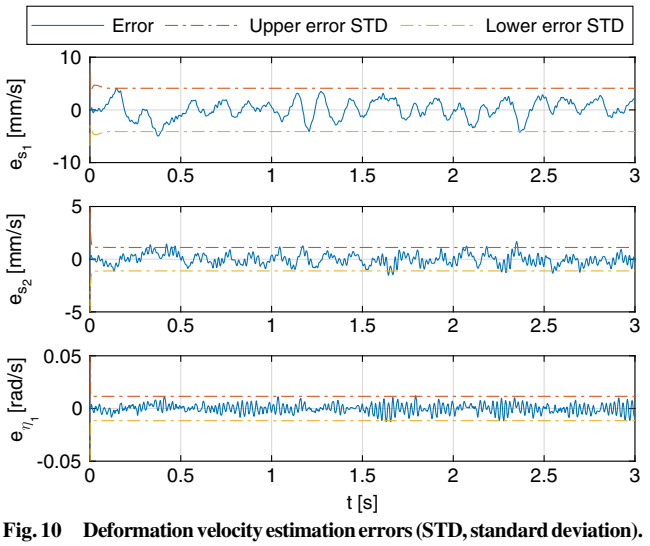

Fig. 10 Deformation velocity estimation errors (STD, standard deviation).

Figure 12 shows the estimated generalized elastic displacements $\boldsymbol{x}_e$. Different from the elastic velocity and acceleration estimations, perceptible errors are present in the displacement estimations. The reason behind this can be revealed by Eq. (32), in which the accelerometer measurements are less correlated with $\boldsymbol{x}_e$. The only term in Eq. (32) that contains $\boldsymbol{x}_e$ is $\widetilde{\boldsymbol{\Phi q}}^T C_w \dot{\boldsymbol{\omega}}_f$, for which the z component is almost zero under small deformations. As a

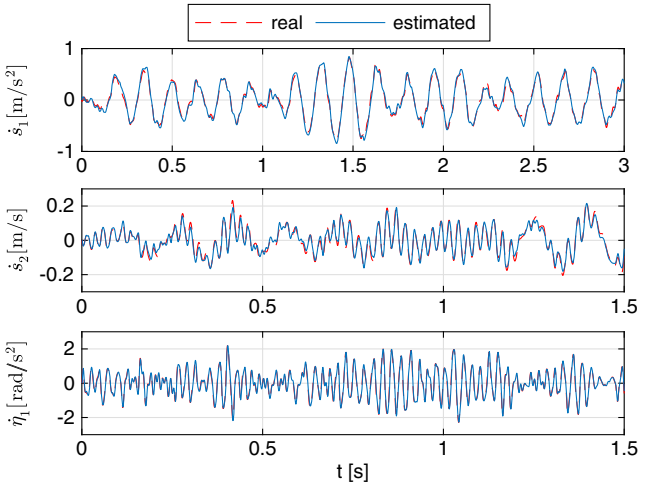

Fig. 11 Real and estimated deformation accelerations.

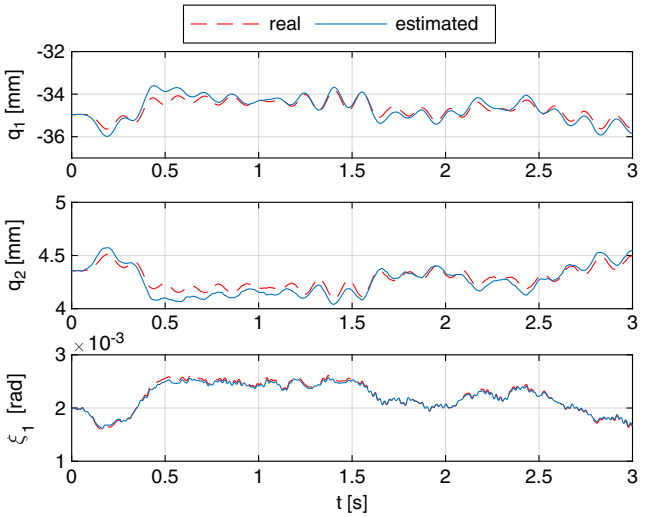

Fig. 12 Real and estimated deformations.

consequence, the estimation of $\boldsymbol{x}_e$ has to depend more on the linearized reduced-order model, which is different from the nonlinear full-order dynamics. Nevertheless, it will be shown in Sec. IV.D that these estimation errors can be tolerated by the INDI control.

D. INDI GLA Simulation Results and Discussions

In this subsection, the INDI GLA control law derived in Sec. III.B will be validated by the benchmark full-order nonlinear flexible aircraft model. This aircraft flies through both a continuous turbulence field (Fig. 3) and a discrete gust field (Fig. 4). The deviation of the vertical load factor from its nominal value $n_z - n_{z_*}$ and the deviations of the wing root bending moment $M_r - M_{r_*}$ are chosen as two performance metrics.

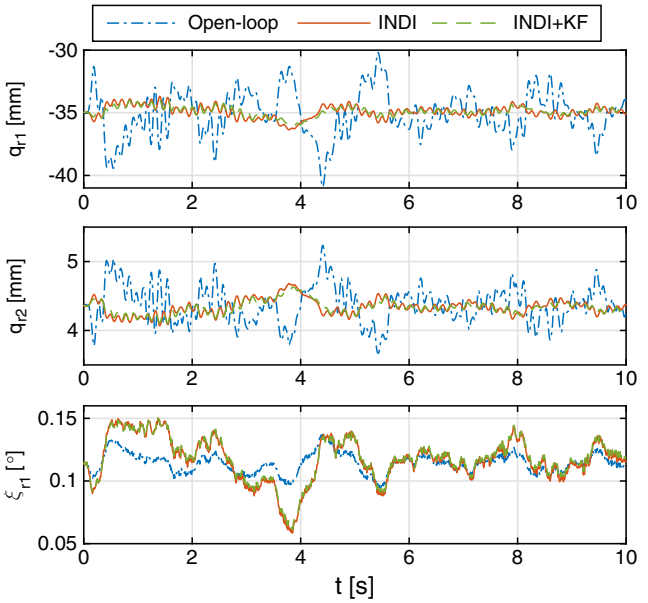

Fig. 14 Generalized displacements under turbulence excitation.

Figures 13–17 illustrate the dynamic responses of the flexible aircraft flying through a von Kármán turbulence field (Fig. 3), in which "open-loop" means responses without control. "INDI" means the closed-loop responses of the system under INDI GLA control, in which the states and their derivatives are assumed to be available. "INDI+Kalman filter (KF)" refers to the closed-loop system responses, when the estimated elastic states and their derivatives are used by the controller. The root mean square (rms) value as well as the peaks of $n_z - n_{z_*}$ and $M_r - M_{r_*}$ are summarized in Table 2. It can be seen from Fig. 13 and Table 2 that the proposed INDI GLA controller effectively alleviates both the vertical load and the wing root bending moment. Because of the unsteady aerodynamic effects, the load responses in Fig. 13 are smoother than the results in Ref. [38], in which the quasi-steady aerodynamics were used. INDI is able to tolerate the state estimation errors (Sec. IV.C) because the closed-loop responses using the estimated states only have small deteriorations as compared to the ideal case.

Figure 15 shows the responses of the generalized elastic displacements, namely, the first bending q_{r_1}, the second bending q_{r_2}, and the first torsion ξ_{r_1} modes of the right wing. For this flexible aircraft configuration, only one set of ailerons is available on the

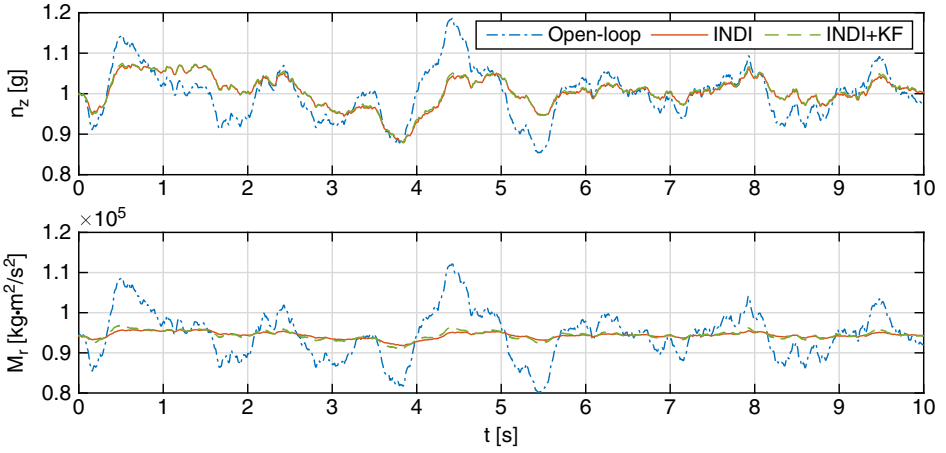

Fig. 13 Vertical load factor and wing root bending moment responses under turbulence excitation.

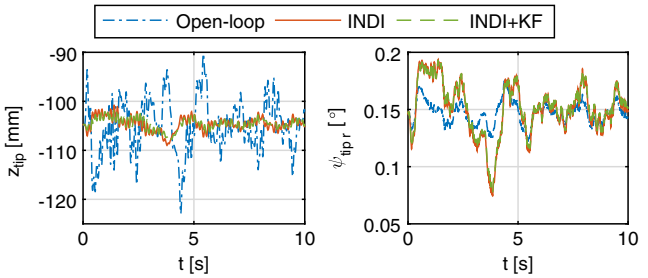

Fig. 15 Wing tip bending and torsion deformations under turbulence excitation.

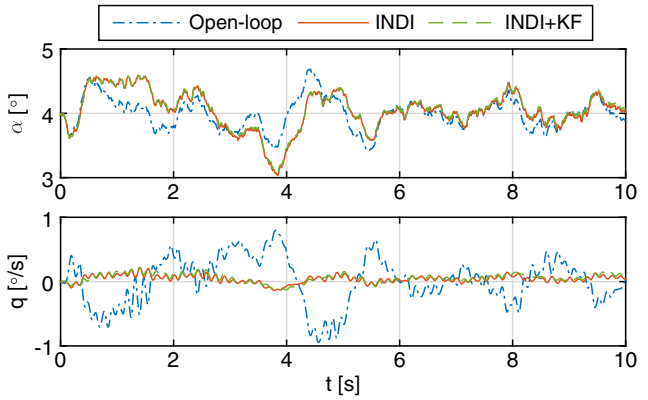

Fig. 16 Rigid-body state responses.

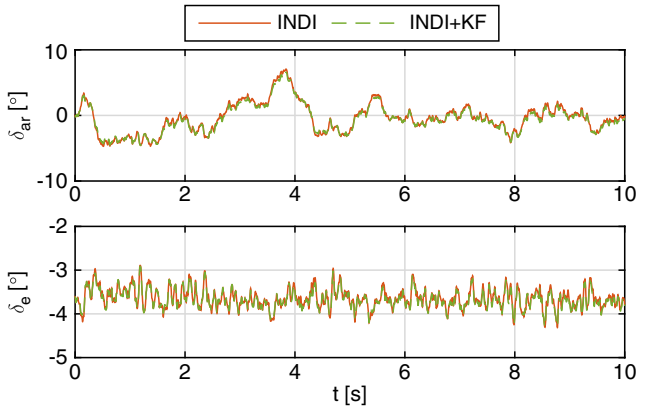

Fig. 17 Control inputs using INDI.

wing, which aims at wing bending and torsion modes suppression, vertical load control, and roll rate control at the same time. However, according to the controllability analysis, this configuration is unable to achieve a decoupled control for all its missions. For example, in the presence of an upwash gust, the wing lift increases, which results in load increment, upward bending, and noseup torsion of the wing, as can be seen in Figs. 18–20. The symmetric up deflections of ailerons would alleviate the wing load and the bending deformation, but they would degrade the torsion deformation because the aerodynamic center of the aileron is behind the wing elastic axis. Because the torsion stiffness is normally larger than the bending stiffness, the vertical load and bending mode control are weighted heavier in Eq. (30). Consequently, as shown in Fig. 14, the bending modes of the flexible wing are successfully suppressed, whereas the torsion deformations have reasonable increments. There are a couple of ways to improve the torsion responses. The fundamental solution would be adding control surfaces (e.g., inboard ailerons, flaperons, spoilers, etc.) to achieve a synergetic control with the outboard ailerons. Novel control surfaces like the variable-camber continuous trailing-edge flap developed at NASA Ames Research Center [9,11] are beneficial for elastic wing controls. It is noteworthy that, from the control design point of view, increasing the number of control surfaces only expands the dimension of the $\boldsymbol{B}_e$ matrix [Eq. (24)]. Stiffening the wing box or increasing the control weights on the torsion motion are also possible approaches.

The wing tip bending and torsion deformations are illustrated in Fig. 15. When using the INDI control, the rms of $z_{\text{tip}} - z_{\text{tip}_*}$ is reduced by 72.6%, whereas the rms $(\phi_{\text{tip},r} - \phi_{\text{tip},r^*})$ is increased by 33% owing to the lack of control surface numbers. Moreover, the rms of the pitch rate is suppressed from 0.37 to 0.07 deg/s. The control inputs are illustrated in Fig. 17, in which the left aileron deflections δ_{al} equal the right δ_{ar} in the symmetric turbulence field.

The dynamic responses of the flexible aircraft in a symmetric $1 - \cos$ gust field (Fig. 4) are illustrated in Figs. 18–21. As shown in Fig. 18 and Table 3. The vertical load factor and wing root bending moment are alleviated by over 36 and 86%, respectively. In the presence of upwash gusts, the ailerons deflect upward symmetrically to alleviate the wing load, as shown in Fig. 22. Analogous to the responses under turbulence excitations, the bending modes are suppressed, whereas the torsion modes have acceptable increments in this gust field, as shown in Figs. 19 and 20. In view of Fig. 21, the peak of the pitch rate q is reduced by 82.7%.

E. Validation by a More Flexible Aircraft Model

As discussed in Sec. IV.A, the benchmark aircraft may not be representative for a very flexible aircraft; thus, a more flexible aircraft model that reduces the stiffness of the benchmark aircraft by 80% is also used to validate the proposed controller. It has been shown in Fig. 7 that the increase of flexibility changes both the rigid-body and elastic modes of the benchmark flexible aircraft. The normal control design routine for this more flexible aircraft would be 1) build a nonlinear reduced-order flexible aircraft model; 2) identify the $\boldsymbol{A}_e$ and $\boldsymbol{B}_e$ matrices in Eq. (30); and 3) retune the control parameters $\boldsymbol{K}_p$ in Eq. (29). In view of the analyses in Sec. III.A, the INDI control is robust to model mismatches by virtue of its sensor-based nature. Therefore, to simplify the implementation process and to assess the robustness of this control, the controller designed for the benchmark aircraft is directly applied to this more flexible aircraft model without modifying the $\boldsymbol{A}_e$, $\boldsymbol{B}_e$, and $\boldsymbol{K}_p$ matrices. During simulations, this more flexible aircraft flies through the 2-D turbulence field shown in Fig. 3 for 10 s. The results are presented in Figs. 23–27, in which "MF" represents "more flexible." As illustrated in Fig. 23, in spite of the model mismatches and the nonoptimal control gains, the maximum value of $n_z - n_{z_*}$ is still reduced by 36.8%. Moreover, the maximum and rms values of the wing root bending moment deviations are, respectively, reduced by 84.7 and 78.3%. The performance of this control can be further improved by using more accurate $\boldsymbol{A}_e$ and $\boldsymbol{B}_e$ matrices and optimizing the control gains.

The generalized displacements and the wing tip deformations are shown in Figs. 24 and 25. When compared to the open-loop responses of the benchmark flexible aircraft (Figs. 14 and 15), this more flexible aircraft has higher vibration magnitude and reduced vibration frequency in the turbulence field. Figure 25 shows that the wing tip of this more flexible aircraft bends up by 551 mm in the trim

Table 2 Maximum and rms values of the load deviation under turbulence excitation

	$\max(n_z - n_{z_*})$, g		$\hat{\sigma}(n_z - n_{z_*})$, g		$\max(M_r - M_{r_*})$, N · m		$\hat{\sigma}(M_r - M_{r_*})$, N · m	
Open loop	0.186		0.0616		1.80×10^4		6.04×10^3	
INDI	0.072	61.3%	0.0386	37.4%	1.63×10^3	90.9%	815	86.5%
INDI+KF	0.074	60.1%	0.0392	36.4%	2.71×10^3	84.9%	1.08×10^3	82.2%

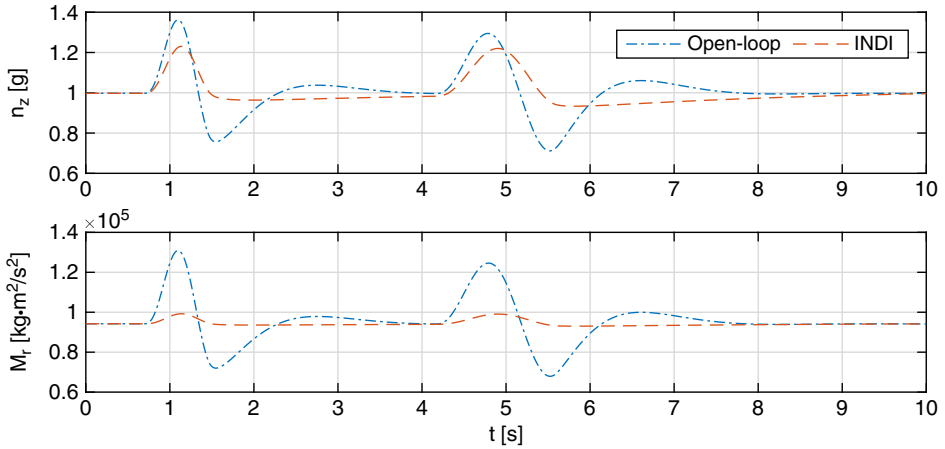

Fig. 18 Vertical load factor and wing root bending moment responses under gust excitation.

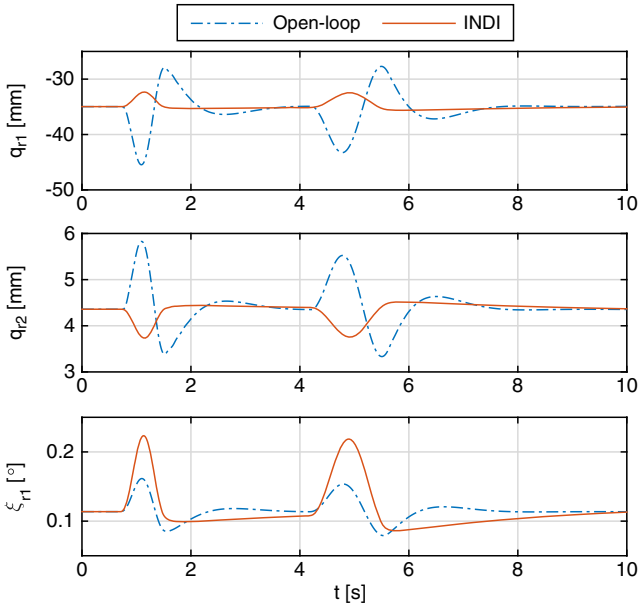

Fig. 19 Generalized displacements under gust excitation.

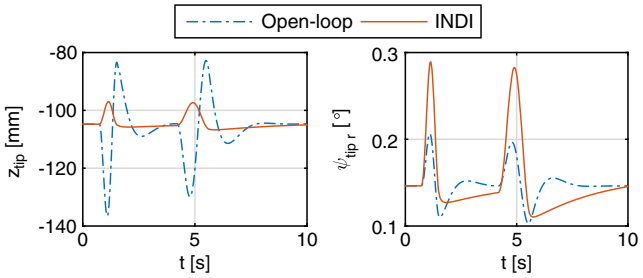

Fig. 20 Wing tip bending and torsion deformations under gust excitation.

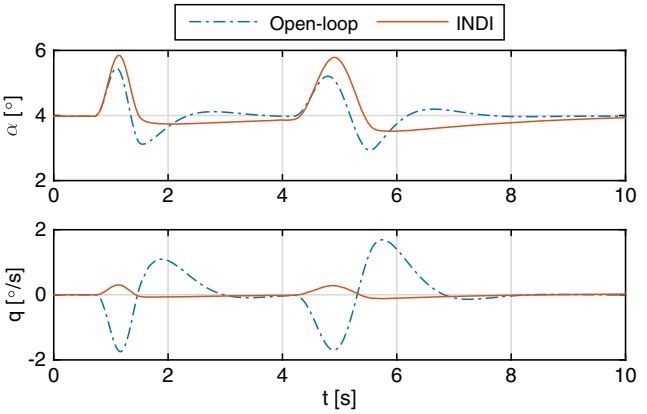

Fig. 21 Rigid-body state responses to gust.

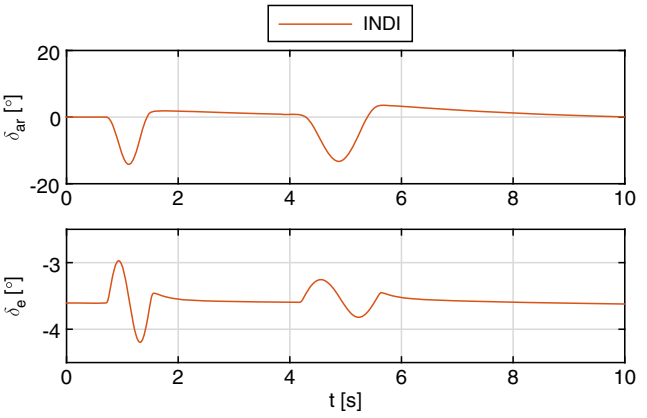

Fig. 22 Control inputs in a gust field.

condition, and it oscillates in the range of $[-606, -508]$ mm under turbulence excitations. The INDI control can reduce the rms of $z_{\text{tip}} - z_{\text{tip}_*}$ by 70.3%. The pitch rate magnitude of this more flexible aircraft doubles the value of the benchmark aircraft (Fig. 16). When INDI is applied, the magnitude of q is reduced from 2.5 to 0.5 deg/s. The control surface deflections are illustrated in Fig. 27.

F. Tolerance to Actuator Faults

As proved in Propositions 1 and 2, the INDI control can passively tolerate actuator sudden faults, provided $\boldsymbol{G}\bar{\boldsymbol{G}}^{-1}$ remains diagonally dominant in the postfault condition. In practice, the tolerance of the control to actuator faults is also constrained by the rate and position

Table 3 Maximum and rms values of the load deviation under gust excitation

	$\max(n_z - n_{z_*})$, g		$\hat{\sigma}(n_z - n_{z_*})$, g		$\max(M_r - M_{r_*})$, N · m		$\hat{\sigma}(M_r - M_{r_*})$, N · m	
Open loop	0.362		0.113		3.67×10^4		1.10×10^4	
INDI	0.231	36.2%	0.070	38.1%	5.10×10^3	86.1%	1.50×10^3	86.4%

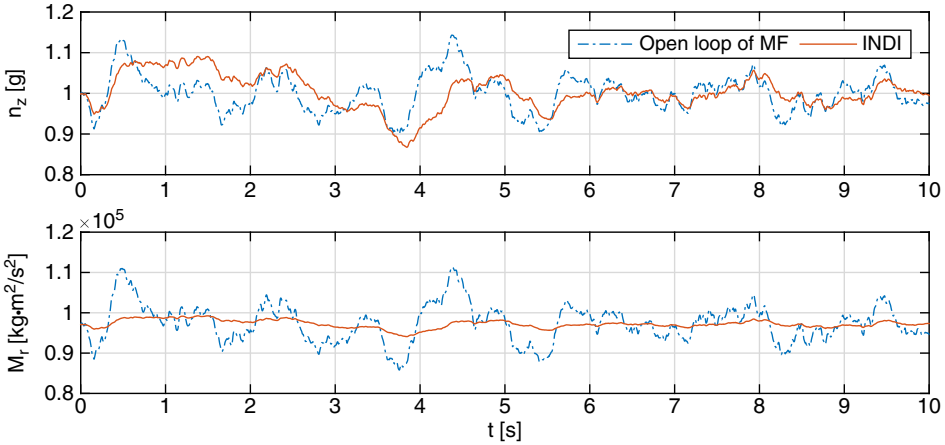

Fig. 23 Load responses of a more flexible aircraft under turbulence excitation.

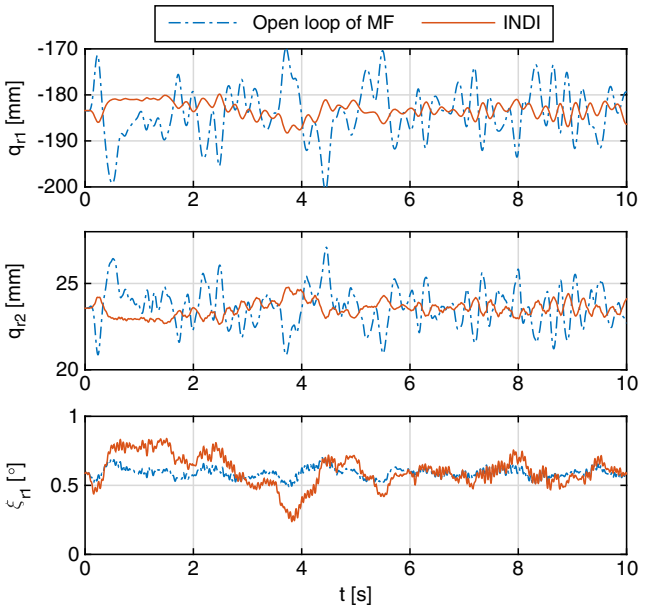

Fig. 24 Generalized displacements of the more flexible aircraft.

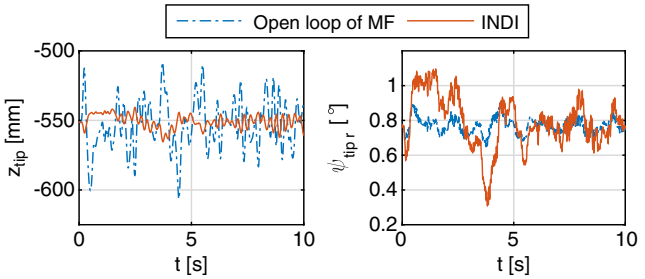

Fig. 25 Wing tip bending and torsion deformations of the more flexible aircraft.

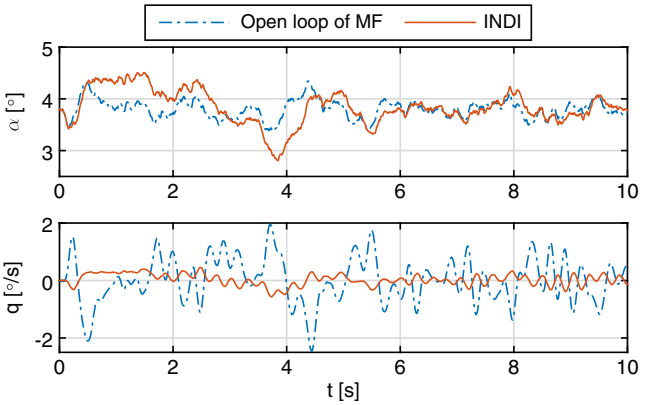

Fig. 26 Rigid-body state responses.

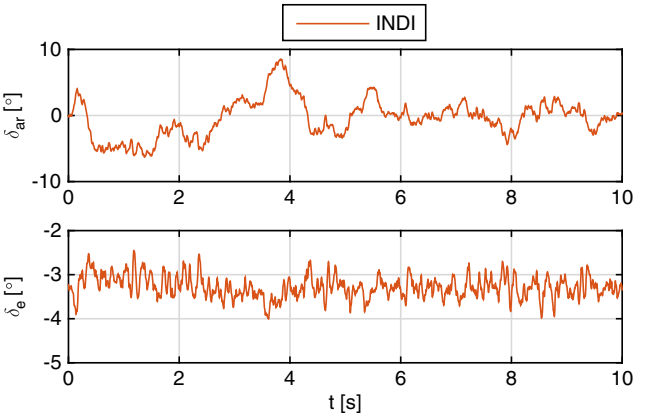

Fig. 27 Control inputs using INDI.

limits of the actuators. In this subsection, a command-filtered actuator compensator is used to handle the actuator nonlinear constraints. The core idea of this technique is that the command given to the actuator is passed through a command filter first, which considers the nonlinear constraints and the bandwidth of the actuator. When the actuator limits are reached, instead of enforcing the actuator to follow the physically unachievable command, an actuator compensator can guarantee the output of the command filter being tracked. For more details of this technique, Ref. [46] is recommended to readers. The pseudocontrol hedging (PCH) technique can also be used to deal with actuator constraints [47,48]. Real-world flight tests have demonstrated the applicability of the combination of PCH and INDI [24].

This subsection will test the robustness of the proposed INDI GLA control to an actuator fault case: partial loss of control effectiveness. When an actuator fault occurs, the circulatory and noncirculatory aerodynamic coefficients related to control deflections in Eqs. (4) and (7) are scaled. However, the control is not aware of the fault, and it still uses the $\boldsymbol{B}_e$ matrix estimated in the nominal case.

Figure 28 shows the load responses of the benchmark flexible aircraft with partial loss of control effectiveness. The label $\sigma_{\Delta M_r}$ is an abbreviation for the rms value of $M_r - M_{r_*}$. During simulations, this aircraft flies through the turbulence field shown in Fig. 3 for 10 s, and all the considered actuator faults occur at $t = 0$ s. As shown in Fig. 28, without changing any control parameter, this controller is able to passively tolerate both ailerons simultaneously losing 50% of their effectiveness. When the fault percentage is larger than 50%, the effectiveness of the control is limited by the rate constraints of the

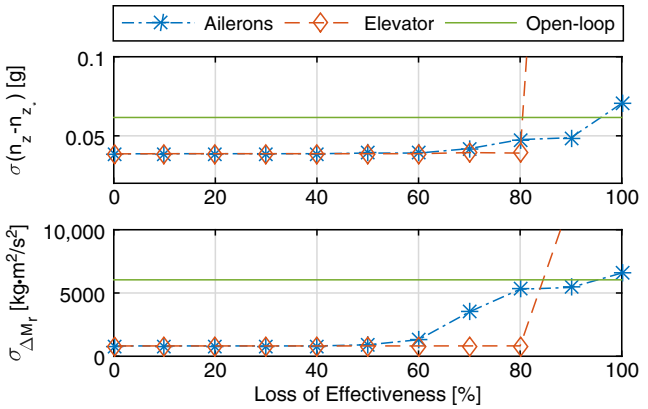

Fig. 28 The rms values of the load deviations in the presence of actuator effectiveness loss.

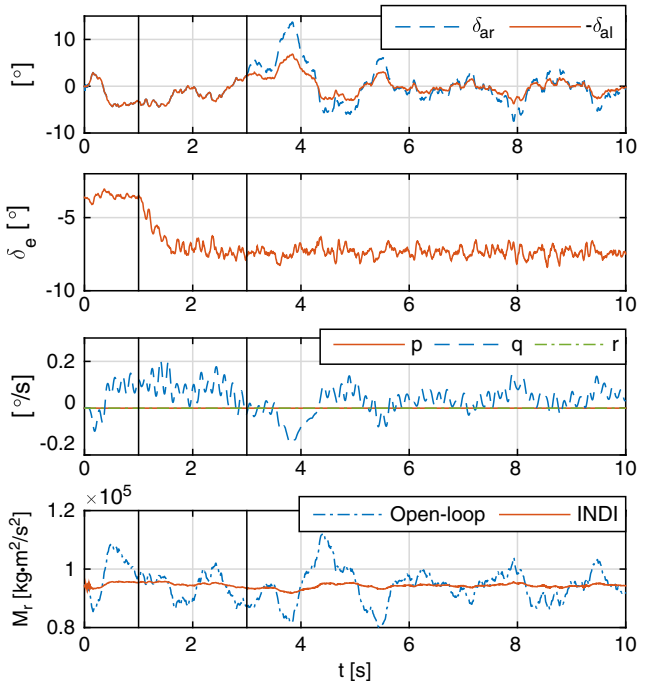

Fig. 29 Half of the elevator and the right aileron effectiveness are successively lost at $t = 1$ s, and $t = 3$ s.

ailerons. The command-filtered actuator compensator can still guarantee the stability, whereas the load alleviation performance inevitably decreases with the increase of fault severity.

Apart from load alleviation, a more important mission of the elevator is to trim the aircraft. As shown in Table 1, the elevator trim angle δ_{e_*} is nonzero in the considered flight condition. As a consequence, when the elevator partially loses its effectiveness, its deflection angle should increase in a timely manner to retrim the aircraft. It can be observed from Fig. 28 that this controller can passively tolerate up to 80% of the elevator effectiveness loss. For more severe cases, the position limit of the elevator is reached, and a retrim becomes physically impossible.

A more comprehensive fault case is illustrated in Fig. 29, in which the elevator suddenly loses half of its effectiveness at $t = 1$ s; following which, 50% of the right aileron effectiveness is also lost at $t = 3$ s. This asymmetrical fault case challenges the lateral retrim ability of this controller. The same as claimed before, neither the model nor the control parameter is modified after the faults occur. In view of Fig. 29, after the elevator fault occurs, the mean value of δ_e doubles in 0.5 s to retrim the aircraft. The deflection angles of the right δ_{ar} and left δ_{al} ailerons are equal before $t = 3$ s (the positive sign is defined as follows: right aileron deflects downward, and left aileron deflects upward). After $t = 3$ s, the magnitude of δ_{ar} increases to compensate for its effectiveness loss. The lateral states p and r are hardly influenced by the faults. As compared to the open-loop responses (Figs. 13 and 16), the rms of q and $M_r - M_{r_*}$ are, respectively, reduced by 80.6 and 86.4% in spite of the faults.

G. Robustness to Aerodynamic Model Uncertainties

As analyzed in Sec. III.A, the INDI control is designed via a sensor-based approach; namely, a part of the dynamic model is replaced by sensor measurements, which improves the robustness of this controller to model mismatches. Regarding flight control, a large proportion of the model mismatches is caused by the difficulties in estimating the aerodynamic coefficients. In view of this, the robustness of the proposed INDI GLA control law to aerodynamic model uncertainties will be evaluated in this subsection.

The flexible aircraft model used in this paper contains k lifting surfaces, namely, the fuselage fu, engine pylon p, wings w, horizontal tail ht, and vertical tail vt. Each aircraft component is divided into n_k strips, and the steady-flow lift curve slope of each strip [$C^{\text{SF}}_{L_\alpha}$ in Eq. (5)] adopts the tabular data in Ref. [2]. In this subsection, this model is augmented by the uncertain parameters $\Delta C^{\text{SF}}_{L_\alpha}$ for robustness validations. It is remarkable that, for the wings and tails, the incorporation of $\Delta C^{\text{SF}}_{L_\alpha}$ also changes the control effectiveness because $C^{c,\delta}_L$ is a function of $C^{\text{SF}}_{L_\alpha}$ [Eq. (7)]. A Monte Carlo simulation containing 1000 uncertain aerodynamic models is conducted, where $\Delta C^{\text{SF}}_{L_\alpha}$ is modeled by

$$\Delta C^{\text{SF}}_{L_\alpha k} \triangleq \left\{\Delta C^{\text{SF}}_{L_\alpha k} \in \mathbb{R} \middle| \Delta C^{\text{SF}}_{L_\alpha k} = N(0, \sigma_k^2)\right\}, \quad \sigma_k = \frac{\rho_k}{n_k} \sum_{i=1}^{i=n_k} C^{\text{SF}}_{L_\alpha i},$$
$$k = fu, p, w, ht, vt \tag{39}$$

For each lifting surface k, the mean value of the uncertainty is zero and the standard deviation σ_k is chosen as ρ_k times the average $C^{\text{SF}}_{L_\alpha}$ of this lifting surface. The perturbation range is chosen as $\rho_{\text{ht}} = \rho_{\text{vt}} = 0.3, \rho_{\text{fu}} = \rho_p = 0.2$ and $\rho_w = 0.1$. As shown in Fig. 30, among all the 1000 samples, the median value of the vertical load factor deviations $n_z - n_{z_*}$ under INDI GLA control is 0.0435 g, which is alleviated by 29.4% as compared to the open-loop value

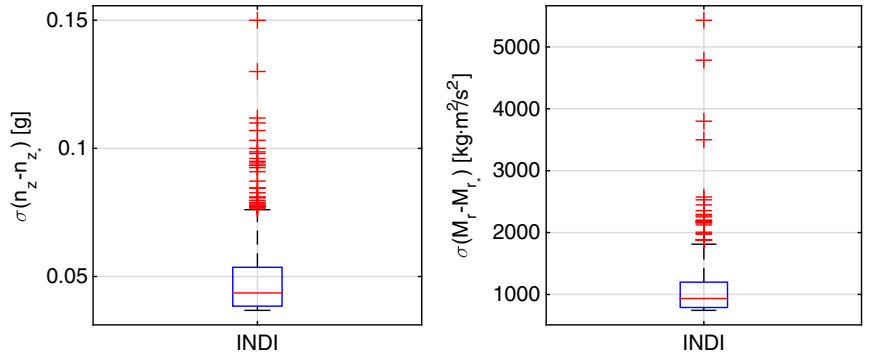

Fig. 30 Box plot of a Monte Carlo simulation of the closed-loop system subjects to model uncertainties.

0.0616 g (Table 2). The interquartile range of $n_z - n_{z_*}$ is only 0.015 g. Moreover, the rms of the wing root bending moment deviations using INDI GLA control is lower than the open-loop value 6405 N · m for all the tested samples. The few larger rms of load variations are caused by dramatic wing lift coefficient perturbations and long-term actuator saturations. This Monte Carlo simulation further verifies the robustness of the proposed controller to aerodynamic model uncertainties.

V. Conclusions

In this paper, an incremental nonlinear dynamic inversion gust load alleviation control law is designed for flexible aircraft. A high-order flexible aircraft validation model is set up, which considers unsteady aerodynamics and encompasses both inertia and aerodynamic couplings between rigid-body and structural dynamics. This flexible aircraft model is compared with a quasi-rigid aircraft model from the perspective of the trim and eigenvalue solutions. The coupling effects lead to different trim solutions for these two models, and they distinguish the rigid-body modes of the flexible aircraft from the modes of the quasi-rigid aircraft. As the wing stiffness reduces, the coupling effects become more prominent. The phugoid mode becomes unstable if the wing stiffness is reduced by 80%.

To simplify the implementation process and reduce the onboard computational load, a reduced-order model is used for control and observer designs. By virtue of its sensor-based nature, incremental nonlinear dynamic inversion (INDI) only needs part of the reduced-order model information. In the presence of model uncertainties, external disturbances, and sudden faults, the residual error of INDI is proved to be ultimately bounded when the conditions in Proposition 1 are satisfied. This bound can be further reduced by increasing the sampling frequency. Provided a bounded residual error, INDI can guarantee the globally ultimate boundedness of the tracking errors (Proposition 2). Due to the lack of control surfaces, the weighted-least squares method is used along with INDI to make tradeoffs among different control objectives. It is shown that the elastic states and their derivatives can be observed from accelerometer measurements using a Kalman filter along with a Padé approximation for modeling the pure time delay.

Time-domain simulations of a full-order flexible aircraft model flying through various 2-D spatial turbulence and gust fields verify that the proposed INDI gust load alleviation (GLA) controller can effectively regulate the rigid-body motions, alleviate the gust loads, reduce the wing root bending moment, and suppress the wing bending modes. The INDI GLA control designed for the benchmark flexible aircraft also shows effectiveness on another more flexible aircraft model without control parameter adjustment. The robustness of the proposed controller is also verified in faulty conditions. It can tolerate sudden actuator faults without using any additional fault detection/estimation method, unless a retrim becomes physically unachievable. Moreover, a Monte Carlo study demonstrates the robustness of the proposed controller to aerodynamic model uncertainties. In conclusion, less model dependency, easy implementation, reduced computational cost, and robustness to external disturbances, sudden faults, and model uncertainties make the proposed INDI control law promising for alleviating the gust loads of flexible aircraft in real life.

References

[1] Meirovitch, L., and Tuzcu, I., "Time Simulations of the Response of Maneuvering Flexible Aircraft," *Journal of Guidance, Control, and Dynamics*, Vol. 27, No. 5, 2004, pp. 814–828. doi:10.2514/1.2392

[2] Meirovitch, L., and Tuzcu, I., "Integrated Approach to the Dynamics and Control of Maneuvering Flexible Aircraft," NASA Langley Research Center CR-2003-211748, Hampton, VA, 2003.

[3] Waszak, M. R., and Schmidt, D. K., "Flight Dynamics of Aeroelastic Vehicles," *Journal of Aircraft*, Vol. 25, No. 6, 1988, pp. 563–571. doi:10.2514/3.45623

[4] Changchuan, X., Lan, Y., Yi, L., and Chao, Y., "Stability of Very Flexible Aircraft with Coupled Nonlinear Aeroelasticity and Flight Dynamics," *Journal of Aircraft*, Vol. 55, No. 2, 2017, pp. 1–13. doi:10.2514/1.C034162

[5] Patil, M. J., and Hodges, D. H., "Flight Dynamics of Highly Flexible Flying Wings," *Journal of Aircraft*, Vol. 43, No. 6, 2006, pp. 1790–1799. doi:10.2514/1.17640

[6] Haghighat, S., Liu, H. H. T., and Martins, J. R. R. A., "Model-Predictive Gust Load Alleviation Controller for a Highly Flexible Aircraft," *Journal of Guidance, Control, and Dynamics*, Vol. 35, No. 6, 2012, pp. 1751–1766. doi:10.2514/1.57013

[7] Fan, W., Liu, H. H., and Kwong, R., "Gust Load Alleviation Control for a Flexible Aircraft with Loss of Control Effectiveness," *AIAA Guidance, Navigation, and Control Conference*, AIAA Paper 2017-1721, 2017. doi:10.2514/6.2017-1721

[8] Dillsaver, M., Cesnik, C., and Kolmanovsky, I., "Gust Load Alleviation Control for Very Flexible Aircraft," *AIAA Atmospheric Flight Mechanics Conference*, AIAA Paper 2011-6368, 2011. doi:10.2514/6.2011-6368

[9] Ferrier, Y., Nguyen, N. T., Ting, E., Chaparro, D., Wang, X., De Visser, C. C., and Chu, Q. P., "Active Gust Load Alleviation of High-Aspect Ratio Flexible Wing Aircraft," *2018 AIAA Guidance, Navigation, and Control Conference*, AIAA Paper 2018-0620, 2018. doi:10.2514/6.2018-0620

[10] Liebst, B. S., Garrard, W. L., and Farm, J. A., "Design of a Multivariable Flutter Suppression/Gust Load Alleviation System," *Journal of Guidance, Control, and Dynamics*, Vol. 11, No. 3, 1988, pp. 220–229. doi:10.2514/3.20297

[11] Nguyen, N. T., Swei, S., and Ting, E., "Adaptive Linear Quadratic Gaussian Optimal Control Modification for Flutter Suppression of Adaptive Wing," *AIAA Infotech @ Aerospace*, AIAA Paper 2015-0118, 2015. doi:10.2514/6.2015-0118

[12] Cook, R. G., Palacios, R., and Goulart, P., "Robust Gust Alleviation and Stabilization of Very Flexible Aircraft," *AIAA Journal*, Vol. 51, No. 2, 2013, pp. 330–340. doi:10.2514/1.J051697

[13] Hodel, A., Whorton, M., and Zhu, J., "Stability Metrics for Simulation and Flight-Software Assessment and Monitoring of Adaptive Control Assist Compensators," *AIAA Guidance, Navigation and Control Conference and Exhibit*, AIAA Paper 2008-7005, 2008. doi:10.2514/6.2008-7005

[14] Khalil, H. K., *Nonlinear Systems*, Prentice–Hall, Upper Saddle River, NJ, 2002, pp. 423–468.

[15] Caverly, R. J., Girard, A. R., Kolmanovsky, I. V., and Forbes, J. R., "Nonlinear Dynamic Inversion of a Flexible Aircraft," *IFAC-PapersOnLine*, Vol. 49, No. 17, 2016, pp. 338–342. doi:10.1016/j.ifacol.2016.09.058

[16] Tewari, A., *Adaptive Aeroservoelastic Control*, Wiley, Chennai, India, 2016, pp. 225–264, 217–254.

[17] Sonneveldt, L., Chu, Q. P., and Mulder, J. A., "Nonlinear Flight Control Design Using Constrained Adaptive Backstepping," *Journal of Guidance, Control, and Dynamics*, Vol. 30, No. 2, 2007, pp. 322–336. doi:10.2514/1.25834

[18] Zhang, Y., De Visser, C. C., and Chu, Q. P., "Aircraft Damage Identification and Classification for Database-Driven Online Flight-Envelope Prediction," *Journal of Guidance, Control, and Dynamics*, Vol. 41, No. 2, 2017, pp. 1–12. doi:10.2514/1.G002866

[19] Sieberling, S., Chu, Q. P., and Mulder, J. A., "Robust Flight Control Using Incremental Nonlinear Dynamic Inversion and Angular Acceleration Prediction," *Journal of Guidance, Control, and Dynamics*, Vol. 33, No. 6, 2010, pp. 1732–1742. doi:10.2514/1.49978

[20] Smeur, E. J. J., Bronz, M., and De Croon, G. C. H. E., "Incremental Control and Guidance of Hybrid Aircraft Applied to the Cyclone Tailsitter UAV," No. 3, 2018, https://arxiv.org/abs/1802.00714.

[21] Sun, S., Sijbers, L., Wang, X., and De Visser, C., "High-Speed Flight of Quadrotor Despite Loss of Single Rotor," *IEEE Robotics and Automation Letters*, Vol. 3, No. 4, 2018, pp. 3201–3207. doi:10.1109/LRA.2018.2851028

[22] Smeur, E. J. J., Chu, Q. P., and De Croon, G. C. H. E., "Adaptive Incremental Nonlinear Dynamic Inversion for Attitude Control of Micro Air Vehicles," *Journal of Guidance, Control, and Dynamics*, Vol. 39, No. 3, 2016, pp. 450–461. doi:10.2514/1.G001490

[23] Smeur, E., De Croon, G., and Chu, Q., "Cascaded Incremental Nonlinear Dynamic Inversion for MAV Disturbance Rejection," *Control Engineering Practice*, Vol. 73, April 2018, pp. 79–90. doi:10.1016/j.conengprac.2018.01.003

[24] Grondman, F., Looye, G., Kuchar, R. O., Chu, Q. P., and Van Kampen, E., "Design and Flight Testing of Incremental Nonlinear Dynamic Inversion-Based Control Laws for a Passenger Aircraft," *2018 AIAA Guidance, Navigation, and Control Conference*, AIAA Paper 2018-0385, 2018.
doi:10.2514/6.2018-0385

[25] Wang, X., Van Kampen, E., Chu, Q. P., and Lu, P., "Stability Analysis for Incremental Nonlinear Dynamic Inversion Control," *2018 AIAA Guidance, Navigation, and Control Conference*, AIAA Paper 2018-1115, 2018.
doi:10.2514/6.2018-1115

[26] Lu, P., Van Kampen, E., De Visser, C., and Chu, Q., "Aircraft Fault-Tolerant Trajectory Control Using Incremental Nonlinear Dynamic Inversion," *Control Engineering Practice*, Vol. 57, Dec. 2016, pp. 126–141.
doi:10.1016/j.conengprac.2016.09.010

[27] Simplício, P., Pavel, M., Van Kampen, E., and Chu, Q., "An Acceleration Measurements-Based Approach for Helicopter Nonlinear Flight Control Using Incremental Nonlinear Dynamic Inversion," *Control Engineering Practice*, Vol. 21, No. 8, 2013, pp. 1065–1077.
doi:10.1016/j.conengprac.2013.03.009

[28] Wang, X., Van Kampen, E.-J., Chu, Q., and Lu, P., "Incremental Sliding-Mode Fault-Tolerant Flight Control," *Journal of Guidance, Control, and Dynamics*, Oct. 2018.
doi:10.2514/1.G003497

[29] Wang, X., Van Kampen, E., and Chu, Q. P., "Gust Load Alleviation and Ride Quality Improvement with Incremental Nonlinear Dynamic Inversion," *AIAA Atmospheric Flight Mechanics Conference*, AIAA Paper 2017-1400, 2017.
doi:10.2514/6.2017-1400

[30] Wright, J., and Cooper, J., *Introduction to Aircraft Aeroelasticity and Loads*, AIAA, Reston, VA, 2007, pp. 157–160.
doi:10.2514/4.479359

[31] Theodorsen, T., "General Theory of Aerodynamic Instability and the Mechanism of Flutter," NACA TR 496, 1935.

[32] Bisplinghoff, R., Ashley, H., and Halfman, R., *Aeroelasticity*, Addison-Wesley, Reading, MA, 1955, pp. 211–260.

[33] Jones, R. T., "Operational Treatment of the Nonuniform-Lift Theory in Airplane Dynamics," NACA TN 667, 1938.

[34] "Flying Qualities of Piloted Airplanes," U.S. MIL-SPEC MIL-F-8785C, 1980.

[35] Etkin, B., *Dynamics of Atmospheric Flight*, Dover, Toronto, 2005, pp. 964–965.

[36] Van Staveren, W., "Analyses of Aircraft Responses to Atmospheric Turbulence," Ph.D. Thesis, Delft Univ. of Technology, Delft, The Netherlands, 2003.

[37] Yang, X., and Zhu, J. J., "Singular Perturbation Margin and Generalised Gain Margin for Nonlinear Time-Invariant Systems," *International Journal of Control*, Vol. 89, No. 3, 2015, pp. 451–468.
doi:10.1080/00207179.2015.1079738

[38] Wang, X., Van Kampen, E., De Breuker, R., and Chu, Q. P., "Flexible Aircraft Gust Load Alleviation with Incremental Nonlinear Dynamic Inversion," *2018 AIAA Atmospheric Flight Mechanics Conference*, AIAA Paper 2018-0774, 2018.
doi:10.2514/6.2018-0774

[39] Cakiroglu, C., Van Kampen, E., and Chu, Q. P., "Robust Incremental Nonlinear Dynamic Inversion Control Using Angular Accelerometer Feedback," *2018 AIAA Guidance, Navigation, and Control Conference*, AIAA Paper 2018-1128, 2018.
doi:10.2514/6.2018-1128

[40] Nam, C., Kim, Y., and Layton, J., "Active Aeroelastic Wing Design for Gust Load Alleviation and Flutter Suppression," *38th Structures, Structural Dynamics, and Materials Conference*, AIAA Paper 1997-1265, 1997.
doi:10.2514/6.1997-1265

[41] Natella, M., Wang, X., and De Breuker, R., "The Effects of Aeroelastic Tailoring on Flight Dynamic Stability," *2018 AIAA/ASCE/AHS/ASC Structures, Structural Dynamics, and Materials Conference*, AIAA Paper 2018-0191, 2018.
doi:10.2514/6.2018-0191

[42] Avanzini, G., Nicassio, F., and Scarselli, G., "Reduced-Order Short-Period Model of Flexible Aircraft," *Journal of Guidance, Control, and Dynamics*, Vol. 40, No. 8, 2017, pp. 2017–2029.
doi:10.2514/1.G002387

[43] Su, W., "Coupled Nonlinear Aeroelasticity and Flight Dynamics of Fully Flexible Aircraft," Ph.D. Thesis, Univ. of Michigan, Ann Arbor, MI, 2014.

[44] Broadbent, E. G., Zbrozek, J. K., and Huntley, E., "A Study of Dynamic Aeroelastic Effects on the Stability Control and Gust Response of a Slender Delta Aircraft," Aeronautical Research Council Reports and Memoranda, 3690, Her Majesty's Stationery Office, London, 1972.

[45] Murua, J., Palacios, R., and Graham, J. M. R., "Applications of the Unsteady Vortex-Lattice Method in Aircraft Aeroelasticity and Flight Dynamics," *Progress in Aerospace Sciences*, Vol. 55, Nov. 2012, pp. 46–72.
doi:10.1016/j.paerosci.2012.06.001

[46] Lu, P., Van Kampen, E., and Chu, Q., "Robustness and Tuning of Incremental Backstepping Approach," *AIAA Guidance, Navigation, and Control Conference*, AIAA Paper 2015-1762, 2015.
doi:10.2514/6.2015-1762

[47] Johnson, E. N., and Calise, A. J., "Pseudo-Control Hedging: A New Method for Adaptive Control," *Advances in Navigation Guidance and Control Technology Workshop*, Redstone Arsenal, AL, Nov. 2000, https://pdfs.semanticscholar.org/7166/d2bac912a1dbb07a3b563037724c5b3c48f3.pdf.

[48] Johnson, E., Calise, A., El-Shirbiny, H., and Eysdyk, R., "Feedback Linearization with Neural Network Augmentation Applied to X-33 Attitude Control," *AIAA Guidance, Navigation, and Control Conference and Exhibit*, AIAA Paper 2000-4157, Aug. 2000, pp. 1–11.
doi:10.2514/6.2000-4157